https://doi.org/10.5194/egusphere-2026-3185
Preprint. Discussion started: 25 June 2026

Continuous Microstructural Characterization of a shallow East Antarctic Ice Core Using Machine Learning Super-Resolution and Micro-CT Imaging

Faramarz Bagherzadeh [1,2], Johannes Freitag [1], Udo Frese [2], and Frank Wilhelms [1,3]

[1]Glaciology, Alfred Wegener Institute, Helmholtz Centre for Polar and Marine Research, Bremerhaven, Germany
[2]Faculty of Mathematics and Computer Science, University of Bremen, Germany
[3]Geoscience Centre, University of Göttingen, Göttingen, Germany

Correspondence: Faramarz Bagherzadeh (faramarz.bagherzadeh@awi.de)

Abstract. This study presents a continuous, high-resolution ($60\mu m$) microstructural analysis of a $130m$ long ice core B40 drilled in the austral summer of 2012/13 at the German Research Station Kohnen on the East Antarctic plateau using deep learning super-resolution, micro-computed tomography (micro-CT), and pore network modeling (PNM). Antarctic ice cores serve as valuable archives of past climate and environmental conditions. They consist of a sequence of compacted layers with varying density, ice, and pore space structure, which are shaped differently depending on the climatic and environmental conditions during deposition and subsequent compaction. The in-depth development of microstructural features provides insights into the densification and pore closure processes as well as climate trends during the formation of the firn column.

However, traditional micro-CT imaging techniques applied to full core samples, although effective, often lack the necessary resolution to capture the intricate microstructure of ice samples fully. To address this limitation, we applied deep learning super-resolution enhancement methods to improve the clarity and detail of micro-CT images, enabling a more precise quantification of ice core properties. Following resolution enhancement, the study performed a comprehensive microstructure analysis on the full firn column, including geometrical, morphological, topological, and transport-related properties. The obtained metrics, including mean intercept length (MIL), cluster size, porosity (density), tortuosity, permeability, etc., can characterize the microstructural evolution of the ice column from snow to bubbly ice across different depths. The results reveal a systematic evolution in pore geometry, connectivity, and transport efficiency with depth, capturing the snow-to-ice transition with high fidelity. Fine and coarse layers were distinguished using the K-means clustering method, and anisotropy was detected in both the ice matrix and the pore space. Principal component analysis (PCA) showed that densification is influenced by multiple factors; in particular, during the pore close-off stage, variations in coordination number and throat dimensions led to distinct densification behaviors among the samples. These findings could contribute to the improvement of densification and air transport models by providing highly accurate data on the microstructure of ice cores and even enabling the definition of new microstructure-related climate proxy parameters.

1 Introduction

Antarctic ice cores are essential tools in climate science, offering a window into Earth's past climate and atmospheric composition across millennia. Ice cores from polar regions, particularly Antarctica, contain trapped air bubbles that preserve ancient atmospheric gases, while variations in the isotopic composition of water molecules record temperature fluctuations over time. These ice cores thus provide unique insights into historical climate changes, including natural cycles of warming and cooling, as well as more recent anthropogenic impacts (Barbante et al., 2010; Jouzel et al., 2007).

The ice archive consists of a succession of layers that were originally deposited as snow. In a process of pressure sintering, the snow compacts into open-pored firn and finally, at the pore close-off depth, into bubbly ice. Firn columns on the Antarctic plateau reach a thickness of approximately $80-110m$ and are characterized by intense layering in density decreasing with depth with a second local maximum close to the firn-ice transition Hörhold et al. (2023); Hoffmann-Abdi et al. (2021) The climate signals preserved in ice cores not only reflect the environmental conditions during snowfall but are influenced by the processes in the firn column, in which extensive mass transport occur during densification (the density increases by a factor of 3 from the surface to the firn-ice transition).

Firn densification occurs through creep in the ice matrix. Several Firn densification models, including empirical, semi-empirical models, have been formulated with different representations of creep and main dependence on temperature T and accumulation rate Salamatin and Lipenkov (2008); Arnaud et al. (1998). With a similar approach Arthern et al. (2010) assume ice deformation according to a Nabarro-Herring creep, including grain growth with the assumption of grain size-dependent densification rates. Freitag et al. (2013) extends the semi-empirical models by introducing an additional softening effect of incorporated impurities (best expressed by the Calcium ion or dust particle concentration) to explain the depth-evolution of the layered structure in density. A recent model approach is using a microstructure-based formulation for compaction to describe viscous densification of firn on the pore scale Fourteau et al. (2023). Gradual pore closure and the transport properties of the open pore space determine the age distribution of the air in the trapped bubbles. Since pore closure depends primarily on density, calculating the gas ages for past climate periods requires reliable densification models Bréant et al. (2017). Densification models have also been used to derive temperatures for the last glacial maximum in East Antarctica by formulating the inverse problem for the input parameter with known firn column heights Buizert (2021). Orbital Dating of ice cores assumes isolation-driven microstructural changes at the surface/snow pack with changes in the ability to trap N2/O2 and air content Bender (2002); Raynaud et al. (1993). The proposed link between the microstructural properties of the surface snow driven by solar radiation and the microstructural properties obtained after compaction at the firn-ice transition, which determine pore close-off, has not yet been confirmed due to a lack of microstructure data.

Analyzing the microstructure of ice cores presents technical challenges, as traditional imaging techniques, such as optical and scanning electron microscopy, cannot capture the three-dimensional (3D) arrangement of internal features effectively. Micro-computed tomography (micro-CT) has emerged as a powerful tool in recent years, allowing researchers to visualize and analyze the 3D internal structures of porous materials non-destructively with resolution of a few microns (Heggli et al., 2009, 2011). In the context of ice core research, micro-CT can reveal the spatial distribution and connectivity of pores, grain

https://doi.org/10.5194/egusphere-2026-3185
Preprint. Discussion started: 25 June 2026

clusters, and inclusions, providing a more complete picture of microstructural properties than 2D methods alone. However, micro-CT imaging resolution is often limited by factors such as scanner capability, sample size, and the inherent trade-off between resolution and field of view. While standard micro-CT methods are capable of capturing features at the micron scale (,i.e. $100\mu m$), they may still miss finer details, particularly in the study of small, delicate pores or thin grain boundaries in polar ice (Hagenmuller et al., 2013).

For studies relying on detailed microstructural metrics such as porosity, tortuosity, and permeability, the limitations of standard micro-CT resolution can significantly impact the quality of the data and the conclusions drawn. Higher resolution imaging is needed to accurately characterize these features and enable precise quantification of the physical properties that govern ice behavior. This resolution is particularly critical for studying ice cores at deeper depths, where compaction increases, and finer structural details may hold vital clues about historical climate conditions and ice sheet stability (Cuffey and Paterson, 2010).

To obtain an accurate digital twin of the scanned samples, it is necessary to perform denoising, segmentation, and pre/post-processing. Early researchers in the field have performed a median filter for noise reduction and a global threshold obtained by bimodal gray-level histograms to segment gray-scale CT of ice core (Freitag et al., 2004; Bagherzadeh et al., 2023). Microstructure parameters are very sensitive to the proper selection of the threshold, as it defines a global structure format. To validate the micro-CT threshold, high-resolution 2D binarized scanning electron microscope (SEM) could be correlated with the 3D micro-CT data (Kerckhofs et al., 2008).

Similarly, Calonne et al. (2022) investigated the effective diffusion coefficient and permeability of firn and snow across a wide density range (100–850 kg/m^3) using samples collected at two Antarctic sites, Dome C and Lock In, along with various laboratory-prepared snow types. Transport parameters were calculated through 3D numerical simulations performed on micro-CT images of the snow microstructure, which allowed precise estimation of gas transport properties. In total, the dataset comprised 152 images, each serving as an independent data point for quantifying and comparing diffusion and permeability across the studied density spectrum.

Also, Bouvet et al. (2023) examined heterogeneous grain growth and vertical mass transfer in snow subjected to a temperature gradient using samples collected from a field site in the French Alps. The study relied on in situ temperature gradient experiments, with snow samples scanned periodically using micro-CT to track 3D microstructural changes over time. Transport parameters and microstructural evolution were quantified through numerical calculations based on these images. In total, the dataset consisted of 72 tomographic images, which provided the basis for analyzing the spatially heterogeneous nature of grain growth and mass redistribution within the snow layer.

Among microstructure parameters, transport properties are among the most important features in ice core analysis, bridging the gap between ice-age gas-age difference, thus researchers try to model the transport properties (permeability and diffusivity) with respect to other parameters for various locations in polar regions. Each model is formulated as a function of open porosity, reflecting the fundamental role of firn microstructure in controlling gas transport properties. Freitag et al. (2002) developed their models based on detailed pore-scale simulations of firn samples from the North Greenland Traverse 1993–95. Their work introduced a power-law relationship for both permeability and diffusivity, providing a consistent theoretical framework over a

https://doi.org/10.5194/egusphere-2026-3185
Preprint. Discussion started: 25 June 2026

wide porosity range. The strength of their approach lies in the fact that it captures the geometric complexity of the pore network using digital image analysis and numerical modeling via lattice Boltzmann models (LBMs).

Similarly, Adolph and Albert (2014) derived their models from direct measurements on firn from Summit, Greenland. These models also take the form of power laws but with different exponents, reflecting site-specific microstructural differences likely driven by higher accumulation rates and warmer temperatures at Summit. Fabre et al. (2000) proposed a linear model for diffusivity based on measurements from both alpine and Antarctic sites, including Vostok, by experimental measurements on firn samples, and using an inverse gas diffusion model. More recently, Fourteau et al. (2019) introduced a power-law model for normalized diffusivity, specifically calibrated on deep Antarctic firn near the LIZ.

Recent advances in artificial intelligence (AI) brought new tools for different scientific applications (Misaghian et al., 2025; Çiftçioğlu et al., 2025; Rizi et al., 2024), and among them, noise reduction and super-resolution imaging techniques offer potential solutions to the resolution limitations of conventional micro-CT imaging. Super-resolution techniques use deep learning algorithms to enhance the spatial resolution of images, allowing finer details to be observed without altering the original imaging setup. In particular, deep learning approaches, such as convolutional neural networks (CNNs) and generative adversarial networks (GANs), have shown significant success in enhancing image resolution across various fields, from medical imaging to materials science (Su et al., 2024; Umirzakova et al., 2024). These methods can effectively interpolate high-resolution features by learning patterns from training datasets, enabling them to reproduce finer details in low-resolution images and improve the interpretability of microstructural characteristics.

In ice core studies, deep learning models that can perform super-resolution (SR) offer an innovative approach to overcoming the limitations of traditional imaging, potentially unlocking finer-scale insights into the structure and composition of ice cores. By applying SR models to micro-CT images, it is possible to achieve higher spatial resolution and contrast, enabling the detection and quantification of microstructural features previously unresolved with standard techniques. For example, super-resolution imaging can clarify pore networks and grain clusters, leading to more accurate calculations of porosity, tortuosity, and permeability (Bagherzadeh et al., 2024a, c). These enhanced measurements can, in turn, improve models of gas diffusion, ice deformation, and other key processes, contributing to a more nuanced understanding of how ice sheets form, age, and respond to environmental changes (Bagherzadeh et al., 2024b).

Research gap:

In the previous studies, researchers obtained a limited number of samples (i.e, every 10 meters) from the firn column. Also, previous studies had to choose a global threshold without proper noise reduction, leading to density errors over 4%. Alternatively, they had to obtain SEM images and fit them with the Micro-CT data to define a better threshold, and this would create a much higher workload. Previous studies also were not able to develop a continuous pore network model, bubble counting, and capturing the connections and clusters within the network, which are crucial parameters for transport-related properties.

Motivation:

This study leverages SR models (trained and validated in our prior study) on top of a continuous ice core micro-CT imaging to provide a high-resolution analysis of Antarctic ice core samples taken from near the surface until a depth of approximately

https://doi.org/10.5194/egusphere-2026-3185
Preprint. Discussion started: 25 June 2026

130 meters, covering the snow-to-ice range. Unlike previous studies, we obtained a complete digital twin of the firn column, and with the help of deep learning SR models, segmented images were generated with less than 2% weight error per 1-meter specimen without the need for secondary measurements such as SEM. Previous studies extracted limited microstructure parameters, whereas in this study, the majority of microstructure parameters, including geometrical, topological, pore network, and transport parameters, are obtained and discussed along the whole firn column. Also, we performed multiple analyses on densification, fine/coarse grain snow, bubble age distribution, and pore close-off zone, which is now possible with continuous microstructural parameters of an ice core.

The primary objective is to improve the accuracy and detail of microstructural measurements for understanding ice core compaction, density changes, and gas retention with increasing depth. By improving image resolution with the help of deep learning SR models, this research hypothesizes that clearer distinctions can be made between microstructural characteristics at various depths, thereby providing new insights into the stages of ice metamorphism and densification that occur under Antarctic conditions. Additionally, this study included a complete analysis of pore network-related features, including coordination number, throat length, and cross-sectional area. Enhanced understanding of these properties is expected to refine models of firn densification and pore enclosure.

2 Material and Methods

The study seeks to extract microstructural parameters of firn cores from CT images. Given the large sample length (approximately $130m$), scanning must be performed at low-resolution using rapid imaging techniques. However, the low-resolution, fast-acquired data introduces various noise effects, which in turn create uncertainties in the CT images.

The SRResNet model was built earlier in our previous paper. In our previous study (Fig.1-left), we performed training/testing of a CNN model for super-resolution (SR) to enhance the resolution and remove the noise. A ResNet-based architecture was selected for this purpose, which is trained and tested on registered low-resolution (LR) and high-resolution (HR) data. Later on, to evaluate the model's effectiveness, metric checks were performed by comparing HR and SR images. Both pixel-wise metrics, such as peak signal-to-noise ratio (PSNR) of 18.2, structural similarity index (SSIM) around 0.74, as well as microstructural metrics, such as permeability and tortuosity percentile error of $5-7\%$, were taken into account. To ensure generalization for the full depth of firn columns (snow-ice), train/test ($75\%/25\%$) samples were selected from different depths. The detailed procedure is in our previous study (Bagherzadeh et al., 2024a, b).

The current study (Fig.1-right) is using the trained model for inference. As data files are extremely large, each image ($120\mu m$) is divided into patches, then fed to the trained SR model, and then the SR outputs are reassembled into a full image ($60\mu m$). Next, these enhanced images undergo unsupervised segmentation (K-means, N_clusters = 2) for binarization. Then the weight calculated from the binary data is compared with the real weight of the specimen, which was measured by an accurate scale in the ice core lab, slightly before imaging.

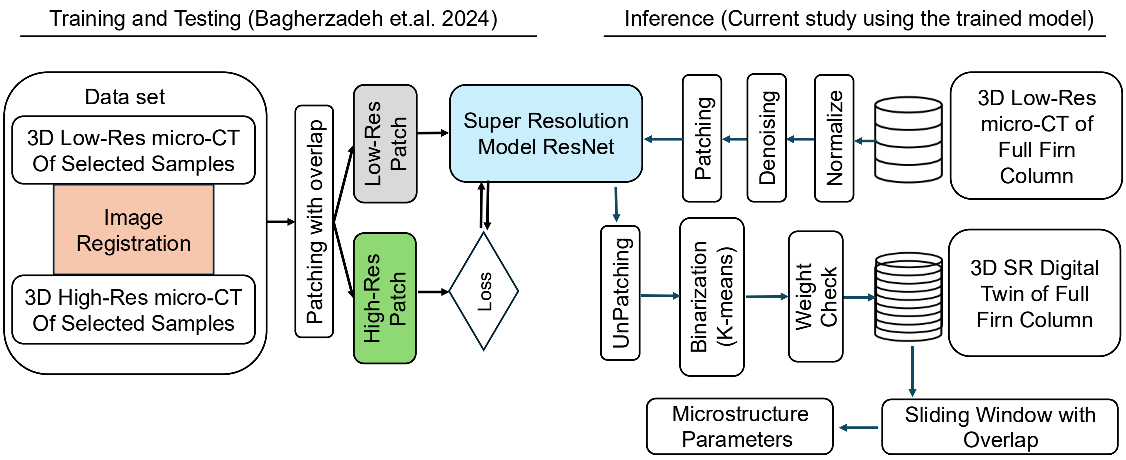

Figure 1. Workflow for the calculation of microstructure parameters from super-resolution ice core micro-CT data. Left-side) train/test of the SR model developed in the previous study; Right-side) The data flow inference used in the current study.

2.1 Dataset

For the continuous microstructure analysis of the firn column, the archived samples of the B40 and B45 firn cores were selected from the AWI ice repository. They are available as half-cores of the originally cylindrical sample segments with a diameter of 10 cm. These ice cores originated from drilling operations in Antarctica in 2012/2013 at Kohnen-Station in Dronning Maud Land (mean annual temperature $-44.6\,^{\circ}\mathrm{C}$ and mean annual accumulation 64 $\mathrm{kg\,m^{-2}\,yr^{-1}}$) in 2012 (Weinhart et al., 2020).

B40 and B45 were drilled $10m$ apart. The uppermost $6m$of B45 were selected due to their superior core quality; B40 archive pieces are selected for the depth range of $6m - 130m$. B40 was dated in a previous study by Sigl et al. (2009) using profiles of stable water isotopes and impurity concentrations (measured by continuous flow analysis, CFA). It will allow future studies to investigate in detail the relationship between impurities, isotopes, and microstructure Sigl et al. (2014).

The selected firn column ice samples are $1m$ ice core segments that were scanned in helical-flyby mode at low resolution (120 mum) using the AWI-iceCT Freitag et al. (2002). The simultaneous vertical movement of the source and detector and the rotation of the specimen, which form a helical path, reduce the scanning time. Due to higher X-ray intensities ($600\mu A$) and smaller pixel detector masks (500×1000 pixels), image exposure times were reduced to $100ms$. Thus, 800 projections were continuously recorded during each rotation, resulting in around 14000 projections per meter of ice core Voland et al. (2010). The reconstructed CT volume images of the target ice core samples were then sent to the data pipeline (Fig.1-right) for inference to produce a digital twin. After generating a digital twin of the selected firn column, a sliding window of (400*400*400 pixels), which is almost $24mm$, is used to compute microstructure parameters continuously along the depth of the ice core, considering 50% overlap. The sliding window was chosen carefully to minimize the inclusion of contaminated samples (such as cracks or breaks). However, in some instances, breaks were still present, requiring a post-processing step. The dataset contains 31 microstructural features, and as the next step, the outliers in key features were removed to preserve data integrity. When a break

https://doi.org/10.5194/egusphere-2026-3185
Preprint. Discussion started: 25 June 2026

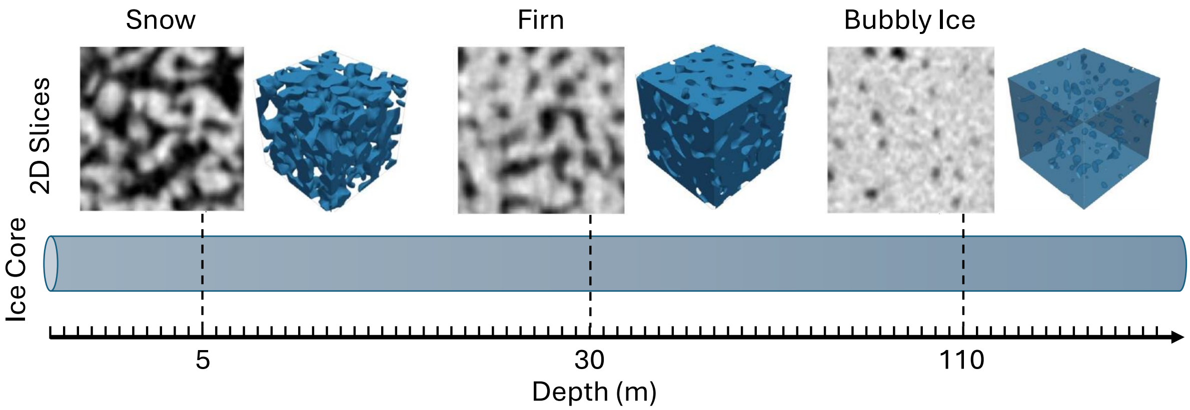

Figure 2. Data set sample from various depth, 2D slices and 3D digital twin

occurs, porosity can increase significantly compared to other samples from the same batch. Similarly, if a thin layer appears, the pore network may exhibit a highly connected pore. These conditions were used as criteria for discarding contaminated samples.

2.2 Microstructural Properties

The SR images were subjected to detailed structural analysis to calculate several key metrics. These metrics help track the changes in ice core microstructure, which are linked to other physical parameters of the ice sheet. Generally, these parameters are divided into three main categories: geometrical and morphological descriptors, transport-related properties, and pore network characteristics.

2.2.1 Geometrical and Morphological Descriptors

Porosity, denoted as ϕ, is defined as the fraction of the total volume of voids (pores) within a material relative to its total volume. It provides a measure of the void space inside the material, which affects properties such as strength, permeability, and thermal conductivity. **Open porosity** refers to the volume fraction of pores that are connected to the external surface of the material, allowing fluids or gases to penetrate the material. Open porosity is important in applications involving filtration, fluid flow, or absorption. It is less than or equal to the total porosity, and it excludes all the isolated bubbles and dead-end throats. Similarly, **Cut porosity** refers to the fraction of pore volume located at or near the sample surface that is connected to only one face (or surface) of the material, resembling dead-end pores that do not connect through to the opposite face.

The **Euler density** is a topological metric that quantifies the connectivity of a binary structure. In this study, we computed the Euler characteristic χ using the `Euler_number` function from the `skimage` module with 3D connectivity set to 3 to consider all 26 neighboring pixels. The Euler number is then normalized by the sample volume (in cm^3) to derive the Euler

https://doi.org/10.5194/egusphere-2026-3185
Preprint. Discussion started: 25 June 2026

density:

$$\text{Euler Density} = \frac{\chi}{V_{\text{sample}}} \qquad where \qquad \chi = C + H - T \tag{1}$$

where C is the number of objects (ice), H is the number of holes, T is the number of tunnels, and V_{sample} is the physical volume of the analyzed sub-volume based on voxel resolution and cube size.

This metric provides insight into the connectivity of pore spaces and solid ice clusters. A more negative Euler density suggests higher topological complexity, indicating more loops and interconnected paths in the void space. This can relate to the mechanical and transport properties of the sample.

The **Specific Surface Area (SSA)** is the surface area of the solid phase per sample unit volume. It was computed using the relevant function from the `PUMAPy` library, which analyzes surface voxels in a binary 3D image Ferguson et al. (2021). The function accounts for voxel resolution to output SSA in units of mm^{-1}:

$$\text{SSA} = \frac{A_s}{V} \tag{2}$$

where A_s is the surface area of the ice matrix and V is the sample volume.

SSA is crucial for understanding processes like heat transfer, vapor diffusion, and metamorphism in snow and firn. Higher SSA values typically correlate with fresher or less compacted snow structures.

The **Mean Intercept Length (MIL)** is a structural descriptor that estimates the average distance a line segment (X, Y, or Z) travels through one phase (ice or pore) before intersecting a boundary. It was calculated using the relevant function from `PUMAPy`, which performs directional ray tracing through the binary 3D matrix (Ferguson et al., 2018). The resulting MIL is a vector MIL $= (L_x, L_y, L_z)$ measured in millimeters.

MIL offers information about **anisotropy** A_z and the average grain size or pore spacing in each principal direction. The results are especially helpful for characterizing snow microstructure and assessing its evolution over time due to metamorphism. In the case of glacier ice (stratified), the anisotropy is primarily governed by the microstructural alignment along the vertical (z) axis, which represents the dominant direction of ice crystal c-axis orientation and fabric development. Because the horizontal plane (x–y) is largely isotropic due to the random distribution of grain orientations and the absence of a preferred structural direction, variations in x and y contribute negligibly to the overall anisotropy. Consequently, anisotropy with respect to the z direction (A_z) provides the most relevant measure of microstructural anisotropy.

$$A_z = 1 - \frac{\mathrm{L}_x + \mathrm{L}_y}{2\,\mathrm{L}_z} \tag{3}$$

The **Spherical Ice Cluster (SIC)** metric represents the mean diameter of the largest spheres that can fit within the ice matrix, weighted by volume. This directly characterizes the shape, compactness, and spatial distribution of ice clusters. The algorithm performs a series of morphological erosions using distance transforms (`scipy`) and computes the reduction in ice volume after each erosion. The cluster diameter D is then averaged:

$$D_{\text{mean}} = \sum_{i=1}^{n} \left(\frac{\Delta V_i}{V_0} \cdot 2r_i \right) \tag{4}$$

where the result of erosion i is the input for erosion $i+1$ and the ΔV_i is the change in volume at erosion step i and r_i is the erosion radius.

This metric captures the compactness and sphericity of solid ice clusters. It is particularly useful for comparing structural differences in compressed vs. fresh snow.

2.2.2 Topological Network Characteristics

Micro-CT images are three-dimensional representations of porous materials, capturing intricate details of their internal structures. These images can be transformed into a pore network model (PNM) by identifying and simplifying the complex geometry into a network of pores (void spaces) connected by throats (narrow pathways). This representation is useful because it allows for efficient simulation and analysis of fluid flow, transport properties, and other physical processes within the porous medium using computationally less intensive models (Fig.3). The Sub-Network of an Over-segmented Watershed (SNOW) is the algorithm that uses a marker-based watershed segmentation to partition an image into regions belonging to each pore. This algorithm, with all the default settings, was used to develop the PNM of our samples.

PNMs have demonstrated considerable potential for accurately predicting the permeability of porous materials when benchmarked against both finite element method (FEM) based simulations and experimental data (Gackiewicz et al., 2021). PNMs were shown to yield permeability estimates that were statistically consistent with those obtained from high-fidelity Navier–Stokes computational fluid dynamics (CFD) simulations across a variety of micro-CT imaged granular media. This finding underscores the ability of PNM to capture essential flow (R2=0.96) characteristics despite its geometric simplifications. Similarly, Wagner et al. (2021) compared multiple numerical methods on idealized regular porous structures and confirmed that PNMs can closely match FEM results, especially in moderately complex geometries. However, while FEM provides higher resolution and geometric fidelity, making it more suitable for highly heterogeneous structures, PNMs offer a favorable balance of computational efficiency and accuracy.

The pore network is constructed using the `snow2` algorithm from `PoreSpy` with default settings, which identifies pores and throats within a binary 3D image Gostick (2017). For a more detailed topological and morphological analysis, various features of the pore network can be extracted. These include the number of pores and throats, the **coordination number** (i.e., the average number of connections per pore), pore and throat diameters, pore volumes, and throat lengths. A pore network is composed of one or more clusters (sub-networks of interconnected pores) where the **cluster size** corresponds to the number of pores it contains. For a given sample, the average cluster size provides an indication of the typical cluster scale, while the **cluster density** represents the number of clusters per unit volume of the sample. Together, these metrics provide a comprehensive characterization of the pore topology and geometry within the ice core. They enable meaningful correlations between the microstructure and the material's transport and mechanical properties, facilitating the classification and comparison of snow microstructures across different samples.

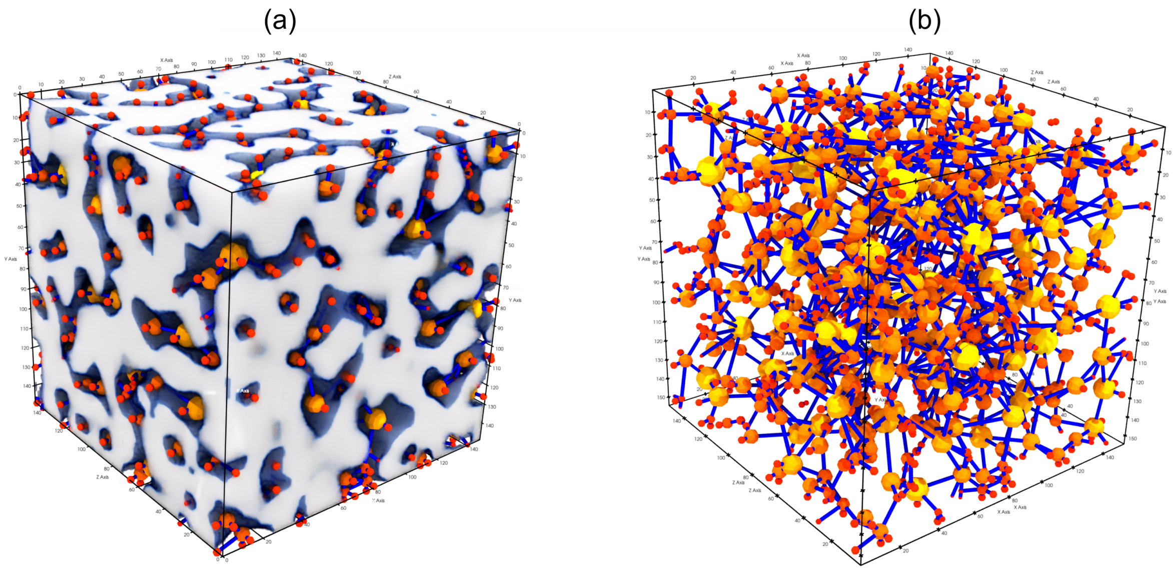

Figure 3. Firn sample visualization a) 3D digital twin obtained from micro-CT b) generated network of pores and throats

2.2.3 Transport-Related Properties

The resulting network from `PoreSpy` is imported into `OpenPNM`, which uses these pore networks and throats with assigned geometrical and physical properties to model and solve problems such as fluid flow, diffusion, and reactive transport. By leveraging the pore network, `OpenPNM` enables efficient and customized simulations that help predict the behavior of porous materials under various conditions, without the high computational cost of directly simulating the full 3D microstructure (Gostick et al., 2019, 2016).

Permeability (k) is computed using pore-network modeling via the `OpenPNM` and `PoreSpy` libraries. After a network is extracted from the binarized pore structure, permeability is calculated by solving Stokes flow across the network (Fig.4.a) using boundary conditions on opposing faces (e.g., z-min to z-max). The formula used is derived from Darcy's Law, assuming unit pressure gradient and fluid viscosity:

$$Q = \frac{k \cdot A}{\mu \cdot L} \Delta P \tag{5}$$

where k is permeability of the medium, μ is dynamic viscosity of the fluid, ΔP is pressure drop across the medium, Q is the volumetric flow rate, L is the sample length, and A is the cross-sectional area.

This approach allows for directional permeability to be estimated in the x, y, and z directions. It offers valuable insights into the fluid transport properties of porous snow and ice microstructures.

Tortuosity (τ) quantifies the complexity of paths through the pore space, defined as the ratio of the actual transport path length to the straight-line distance. In this work, tortuosity is computed using a diffusive simulation through the pore network (Fig.4.b), also built using `PoreSpy` and analyzed with `OpenPNM`. The effective diffusivity D_{eff} is computed under set

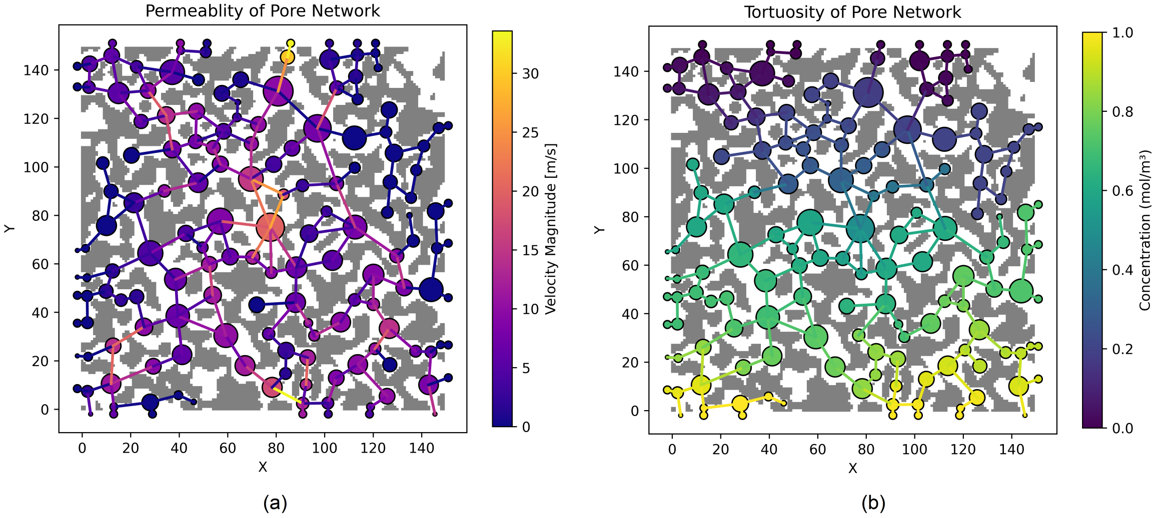

Figure 4. Transport properties on 2D sample network a) velocity field for permeability calculation b) concentration field for tortuosity calculation

boundary conditions and compared to the free diffusivity D_0:

$$\tau = \frac{\phi \cdot D_0}{D_{\text{eff}}} \qquad where \qquad D_{\text{eff}} = \frac{N_A \cdot L}{A \cdot \Delta C} \tag{6}$$

where ϕ is porosity, D_0 is intrinsic diffusivity of air ($1.6 \times 10^{-5}\,\text{m}^2/\text{s}$), and D_{eff} is computed from Fickian diffusion simulations, L is length of sample, N_A is molar flow rate, A is cross section, and ΔC is concentration difference. Tortuosity gives insight into the impedance faced by gases moving through the structure. Higher tortuosity suggests more convoluted pathways and reduced transport efficiency.

3 Results and Discussion

As described earlier in Sec.2, raw micro-CT data of the firn column were passed to a deep learning model for super-resolution and noise reduction, and then it was segmented with an unsupervised algorithm. A 3D window of 400 with 50% overlap was running over this data to obtain microstructure parameters. The following results are obtained.

3.1 Geometrical Properties of Firn Microstructure

The total porosity of the ice core samples exhibits the expected clear decreasing trend with depth in accordance with the opposite trend in density (Fig.5.a, 6.a). Near the surface, porosity is relatively high (around 55%), reflecting the loosely packed structure of freshly deposited snow (Fig.5.a). As depth increases, porosity declines progressively, indicating densification due to overburden pressure and metamorphic processes. This compaction results in a more consolidated ice matrix. The quadratic

https://doi.org/10.5194/egusphere-2026-3185
Preprint. Discussion started: 25 June 2026

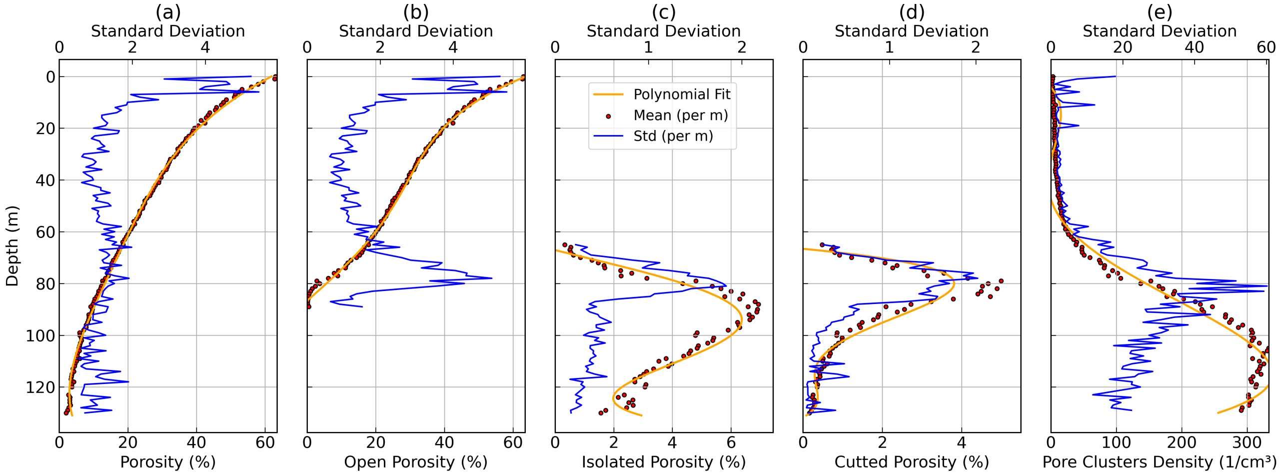

Figure 5. Porosity related parameters averaged per meter over the depth: a) total porosity, b) open porosity, c) isolated porosity(bubbles), d) cut porosity (dead-end paths), e) number of separated clusters appeared in the pore network model per unit volume.

fit with narrow standard deviation bounds suggests a systematic and consistent densification trend within the studied depth range.

Open porosity shows a similar trend to total porosity, with values decreasing with increasing depth (Fig.5.b). The initial high open porosity values correspond to a permeable firn structure near the surface, which facilitates gas transport. With depth, open pores collapse or become isolated, leading to a significant reduction in open porosity. The well-defined curvature of the quadratic fit captures the transition from permeable firn to more compact and less interconnected ice layers, highlighting the progressive pore closure, and at a depth of $90m$, there is no open porosity.

Isolated porosity appears around $62m$, and it increases with depth until around $95m$, beyond which it decreases sharply (Fig.5.c). This reflects the closure of open pores and formation of isolated air bubbles due to continued compaction and sintering. The peak in isolated porosity marks the depth at which the transition from open to closed porosity is most active. This behavior is consistent with the firn–ice transition zone, where air becomes trapped within the ice matrix. After $95m$, the bubbles begin to shrink, thus reducing the isolated as well as total porosity.

Cluster density represents the number of connected network clusters from the pore-network model (Fig.5.e), where on the upper part of the ice core, the whole network is connected, and only 1 cluster exists. Between depths of $40m$ and $60m$ there are some samples with more than one cluster, but there is no isolated porosity (Fig.5.c) which indicates the presence of multiple paths that are open but not connected to each other. With increasing the depth ($60m$ to $90m$), more separated clusters appear and isolated clusters increase, which is an indication of forming new bubbles. In deeper samples, the main permeable cluster shrinks and divides into isolated bubbles, and the number of bubbles constantly increases till a depth of $110m$. After this depth, the number of clusters is decreasing due to bubble shrinking, so the bubbles become smaller than the resolution of our CT

https://doi.org/10.5194/egusphere-2026-3185
Preprint. Discussion started: 25 June 2026

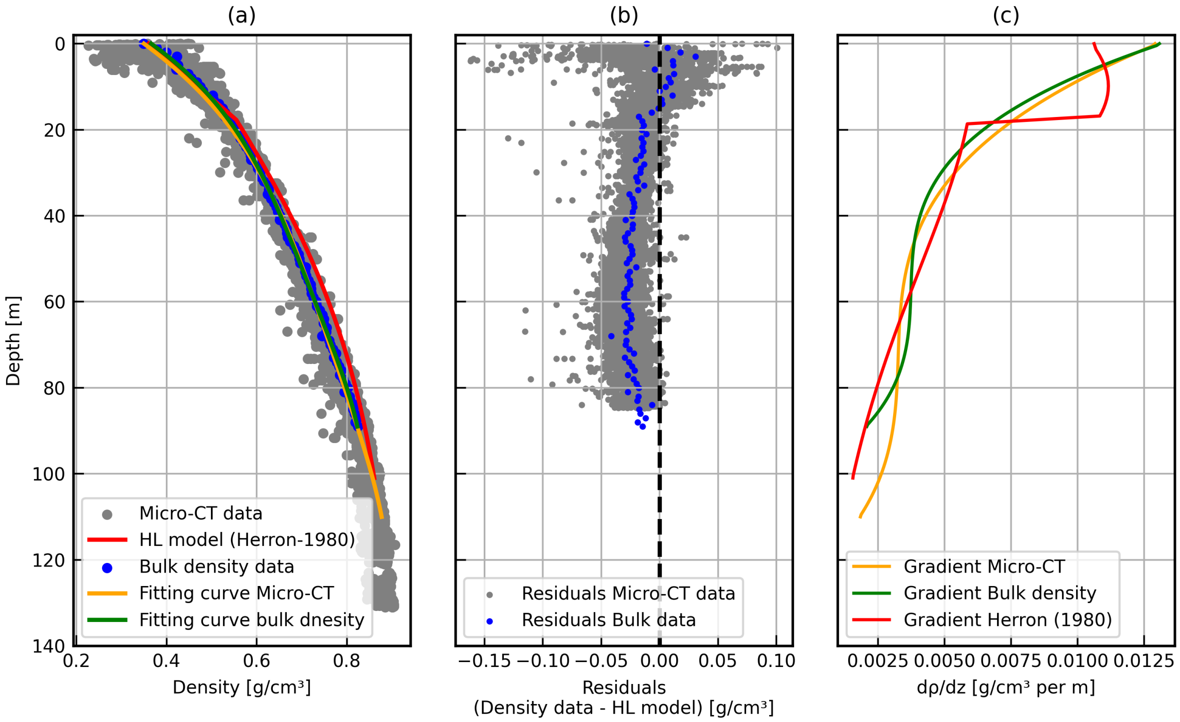

Figure 6. Firn Densification at Kohnen Station

images. On the deeper part of the firn, pore cluster density represents the Bubble density (almost 300 bubbles per cm^3), and it is well in agreement with other investigations of this region (Bendel et al., 2013).

The Herron and Langway Jr (1980) firn densification model is a widely used semi-empirical approach to describe how snow compacts into firn and eventually ice as a function of depth, temperature, and accumulation rate. The model is based on two stages of densification: the first dominated by grain boundary sliding until the critical density of approximately $0.55,\mathrm{g/cm^3}$ is reached, and the second governed by power-law creep processes until pore close-off. In this study, we applied the Herron and Langway model using the site-specific parameters of firn temperature ($T = -44.6,^\circ\mathrm{C}$), annual accumulation rate ($A = 66.2,\mathrm{mm,w.e.,a^{-1}}$), and surface density ($\rho_0 = 0.360,\mathrm{g/cm^3}$). To evaluate the model performance, we measured the bulk density of the ice core and compared these measurements with density estimates obtained from high-resolution SR micro-CT scans. The results show that while the Herron and Langway model captures the overall densification trend with depth, the bulk density measurements and micro-CT data provide more detailed insight into local variations in firn structure. In particular, the micro-CT data reveal fine-scale variability that is not resolved by bulk density measurements but aligns well with the general densification pathway predicted by the model.

The Herron and Langway model reproduces the general trend of firn densification, with density increasing smoothly with depth until close-off (Fig.6.a). The bulk density values fall close to the model curve, but the micro-CT data reveal significantly

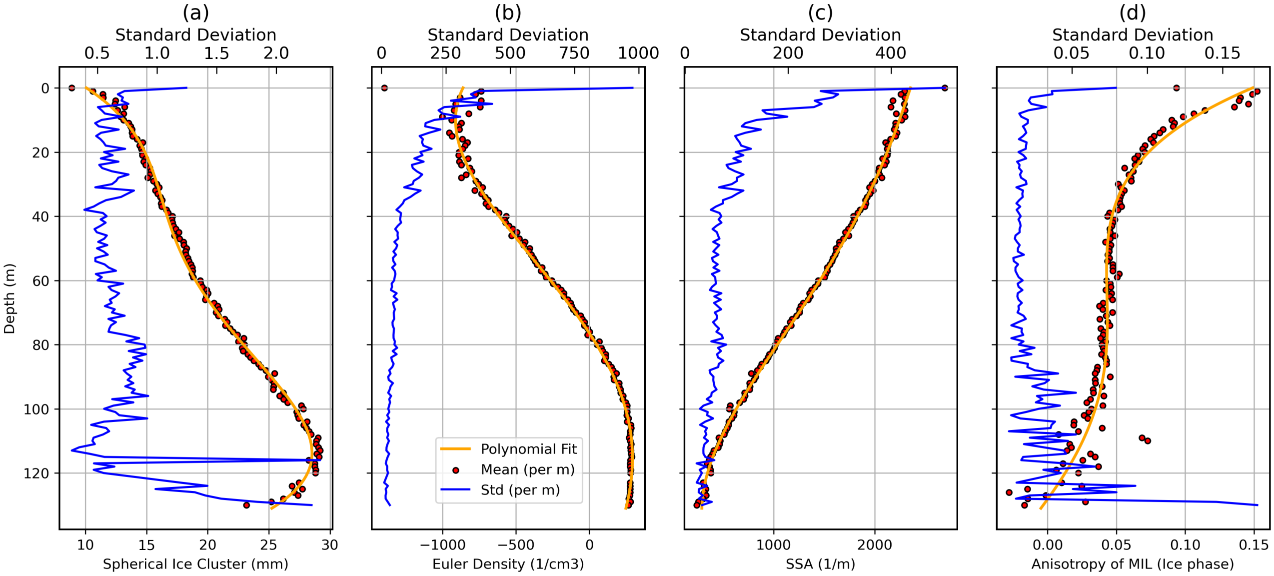

Figure 7. Geometrical properties over depth a) spherical ice cluster measured in ice domain b) Euler density c) specific surface area(SSA) d) anisotropy of mean intercept length(MIL) measured in ice domain

more scatter, reflecting the heterogeneity of firn microstructure at the millimeter scale. This comparison highlights how the model captures the large-scale behavior, while micro-CT resolves the small-scale variability that bulk methods average out.

To better assess the agreement between model and data, Fig.6.b,c show the residuals and densification gradients, respectively. The residuals (Micro-CT minus model) are centered close to zero but exhibit systematic deviations with depth, particularly in the upper firn, where densification is more variable. The densification gradient (dρ/dz) shows the rate of compaction, with the micro-CT data showing greater variability compared to the smoother model prediction. These plots emphasize that while the Herron and Langway model provides a good first-order estimate of firn densification, local processes and small-scale heterogeneities captured by micro-CT imaging contribute to deviations that are not fully resolved by bulk density or semi-empirical models.

As shown in Fig.7.a the size of spherical ice clusters increases with depth, suggesting grain growth and recrystallization processes. Near the surface, smaller ice clusters are prevalent, indicative of initial snow structures. With increasing depth, the microstructure coarsens as grains grow and reorganize in the ice phase. Similarly, Euler density, representing the topological connectivity of the pore phase, increases with depth (Fig.7.b). High Euler density values near the surface reflect a complex, interconnected pore structure typical of fresh snow and firn. As depth increases, this connectivity diminishes due to pore collapse and closure, resulting in fewer connected pathways. The downward trend supports the interpretation of increasing isolation and pore simplification as compaction progresses.

Specific Surface Area (SSA) decreases with depth, indicative of grain coarsening and loss of fine microstructural features (Fig.7.c). At shallow depths, high SSA values correspond to highly porous structures with numerous interfaces. With metamor-

https://doi.org/10.5194/egusphere-2026-3185
Preprint. Discussion started: 25 June 2026

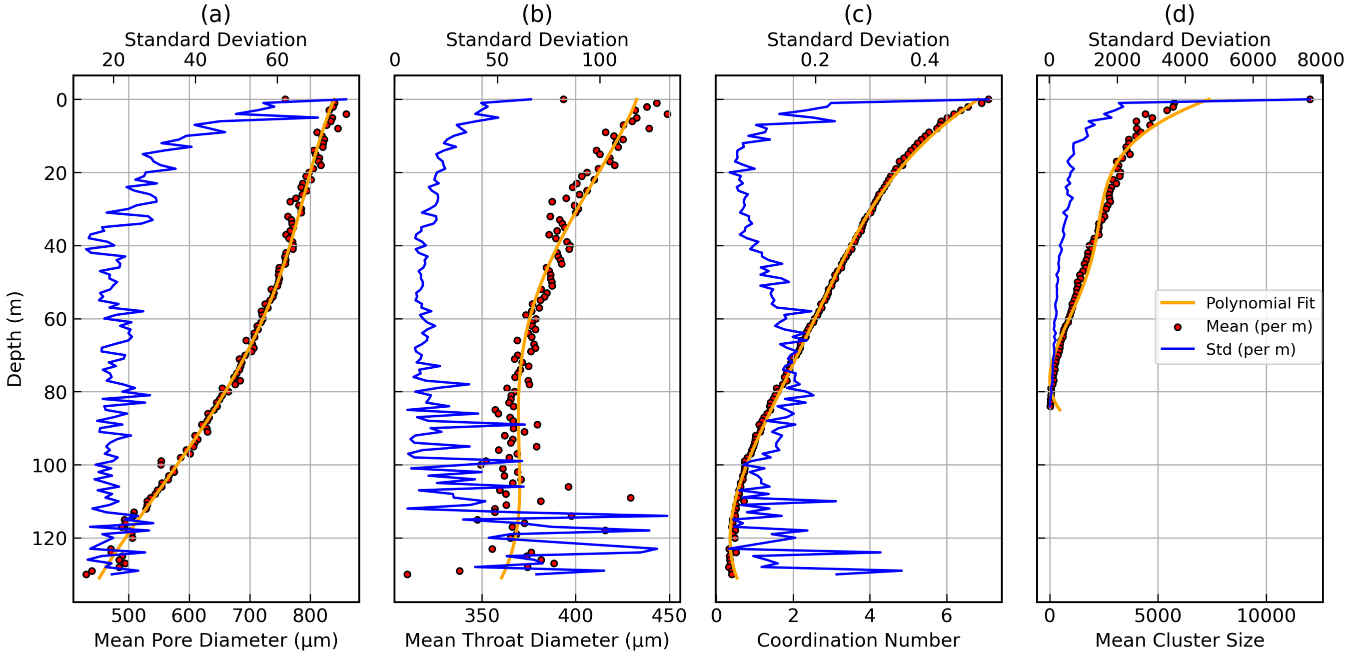

Figure 8. Network properties over depth: a) mean pore diameter, b) mean throat diameter, c) coordination number, d) mean cluster size (cluster size = number of pores in one cluster)

phism, the surface area reduces due to grain growth and loss of microstructural complexity. This decline in SSA is a critical factor in understanding changes in gas diffusion. Also, the mean intercept length anisotropy in the Z-direction decreases with depth, reflecting depth-related elongation reduction vertically in ice phase (Fig.7.d) specifically with a sharp slope between surface and $15m$depthsdepths depth. This range corresponds to the convection range. At deeper depth, the MIL anisotropies reduce, where the main process of gas exchange is diffusion. The variation of this parameter in the depth range $85-130m$ suggests that pore elongation may happen for different samples depending on the stress applied to them.

3.2 Pore Network Topology and Connectivity of Firn Microstructure

As shown in Fig.8.a, the mean pore diameter decreases with depth, indicating that as the ice compacts, the bigger pores near the surface become smaller and some of them disappear (Fig.8.d). This trend likely reflects coarsening processes and the sintering of adjacent grains, which reduce surface curvature. Similarly, the mean throat diameter and coordination number (Fig.8.b,c) decrease over the depth, indicating that as the depth increases, throats become smaller and disappear, so the coordination number is also reduced. This reduction and loss of connections is more severe in the top $15m$ of the firn column (convection zone).

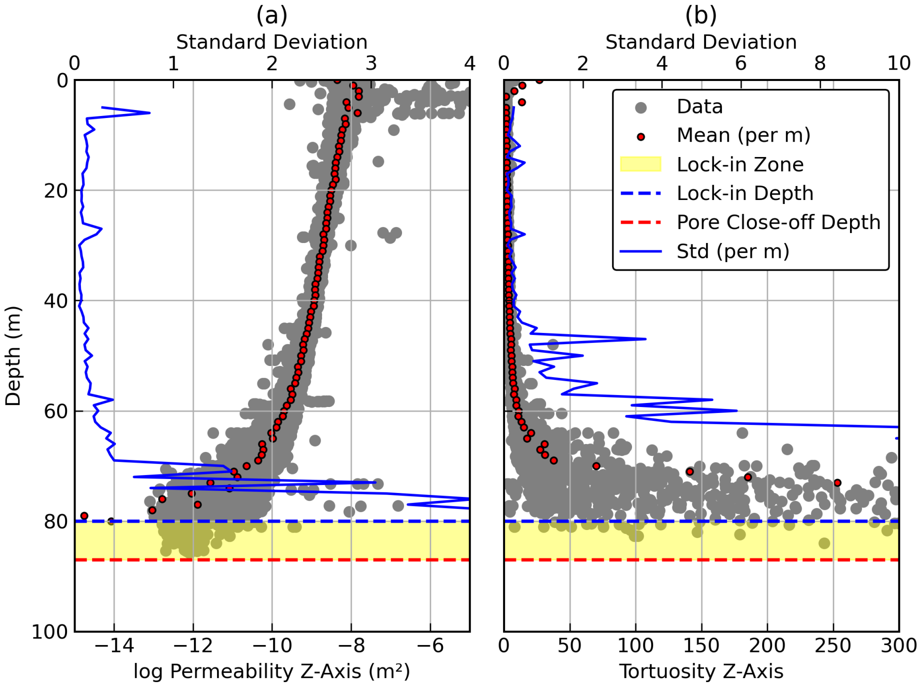

Figure 9. Transport properties along depth a) permeability b) tortuosity

3.3 Transport Properties and Pore Close-off

The key microstructural transport parameters, permeability and tortuosity, are shown in Fig.9.a along the depth. These parameters play a crucial role in determining gas transport properties within firn and ice, impacting the interpretation of ice core gas records. At Kohnen Station (where samples are collected), a high-elevation East Antarctic site, low temperatures and high accumulation rates result in a relatively deep and slow densifying firn column (densification process proceeds gradually). The location's climatic conditions promote slow firnification, leading to a more extended transition zone where gas trapping occurs over a vertical depth range; therefore, the permeability and tortuosity transitions occur gradually.

As shown in Fig.9.a, permeability decreases nonlinearly with increasing depth. Near the surface (snow layers until $10m$ depth), values are relatively high, reflecting the open and interconnected pore structure characteristic of unconsolidated snow and firn. This part of the firn column has the highest permeability (Fig.9) and anisotropy (Fig.7.d) because at this depth (**convective zone**) the means of air transport is convection that happens due to wind and temperature difference (Kawamura et al., 2006). As depth increases, compaction driven by overburden pressure reduces pore space and connectivity, thus reducing permeability. In this stage, molecular diffusion is the main transport mechanism (**diffusive zone**). The permeability curve steeply drops and approaches zero, which is typically around $60\breve{}100m$ in East Antarctic sites (Battle et al., 2011). Similarly, tortuosity (Fig.9.b) increases with the depth. Near the surface, low tortuosity values suggest relatively straight, open pathways.

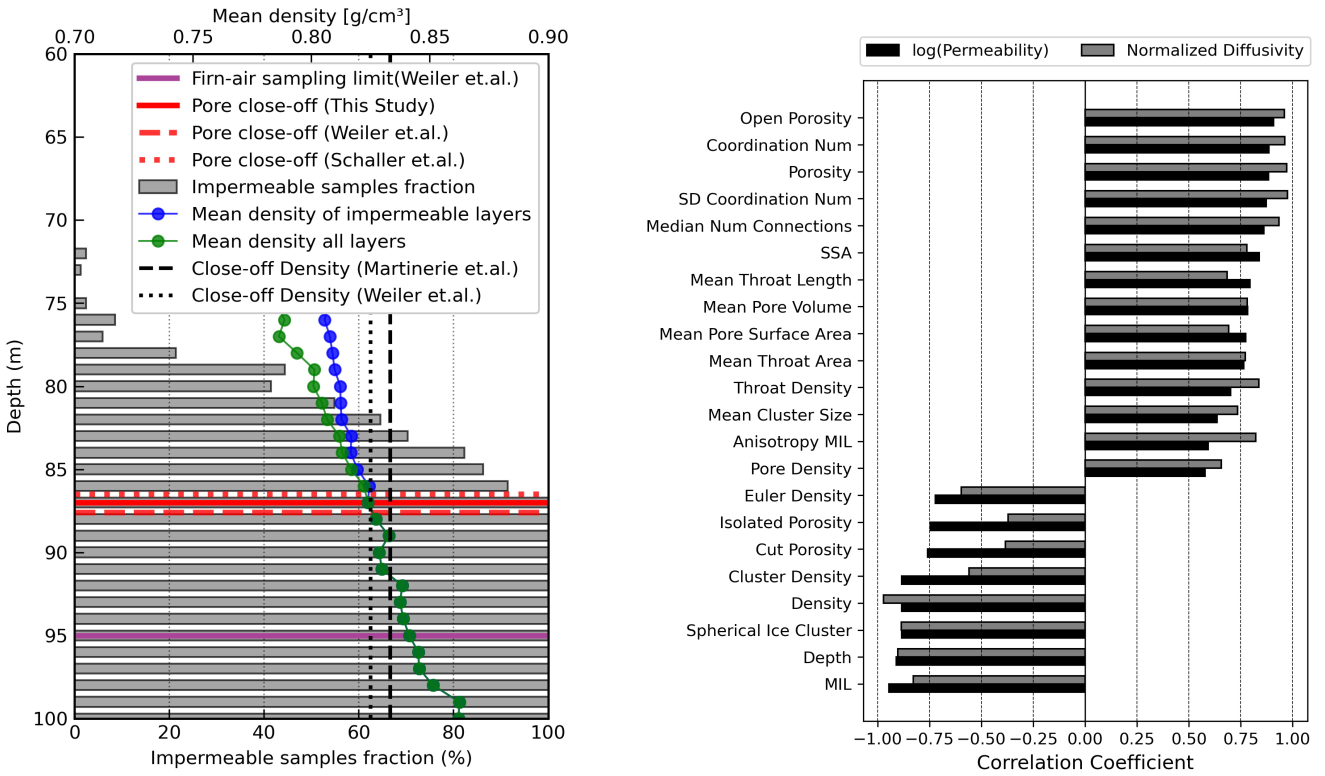

(a) (b)

Figure 10. Permeability range and feature relevance: a) Fraction of impermeable layers per meter of depth; b) Feature correlation with transport parameters.

With depth, tortuosity increases as pore channels become more constricted and indirect, specifically after depth of $65m$, the paths become extremely complex.

As illustrated in Fig.5.b, the open porosity approaches zero, indicating **pore close-off** at a depth of approximately $87m$, which is the final depth (Fig.9) for permeability and tortuosity as well. Similarly, with more details, Fig.10.a shows the fraction of impermeable layers in each meter of ice sample. In depth around $86m$, more than 90% of sub-samples are impermeable, and the average density is $0.824g/cm^3$. This value is very close to the prior investigations in literature that refer to a close off density (ρ_{co}) that happens at $0.825g/cm^3$ and $0.833g/cm^3$ as a reference point (Weiler, 2008) and (Martinerie et al., 1992) respectively. The lock-in depth (**LID**), where the first significant impermeable firn layers begin to inhibit air diffusion, could be assumed to occur around $81m$(Fig.10.a) with an over 1m averaged density of $0.81g/cm^3$ with around 50% blocking samples. Then the interval between these two depths (81 to $87m$) is known as the lock-in zone (**LIZ**), characterized by alternating permeable and impermeable layers (Fig.9.a). Below the close-off depth, permeability effectively drops to zero, as air becomes fully enclosed in sealed bubbles within the ice matrix (Gregory et al., 2014).

Weiler (2008), focused on the composition of firn air with combined high-resolution firn air sampling at Kohnen Station (Antarctica) with diffusion–temperature modeling. Weiler (2008) determined the pore close-off depth from density profiles, applying the criterion of $\rho_{co} \approx 0.825 g/cm^3$, which gave $87.6m$ (Fig.10.a). They performed an air extraction experiment, and above the close-off depth, air could be drawn efficiently, but below this depth, the yield declined rapidly, as only small amounts of isolated air remained accessible through the borehole connection. At this depth, effective diffusivity dropped to zero. Using a bladder-tube pump, they still extracted firn air down to $94.9m$(Fig.10.a), though the flow declined significantly (Opel et al., 2009; Kipfstuhl et al., 2009). On the other hand, Schaller et al. (2017) studied a similar core in the nearby region (B49 & B53) with high-resolution ($29\mu m$) micro-CT data. They concluded that a total porosity of 0.1 (density 0.825) is the critical value leading to a close-off depth of $86.5m$, and air pumping experiments on the region were still able to pump out air within a few meters below this depth.

In comparison with these studies, our dataset indicates pore close-off at a depth of approximately $87m$. According to the literature, however, a nearby pumping experiment was able to extract air down to $94.9m$ (Weiler, 2008). Despite the successful air extraction reported there, our measurements do not reveal any open pores at those depths, which necessitates several explanatory assumptions. One possibility is that the pumping experiment exerted sufficient pressure on the ice to reopen very small channels temporarily. Another consideration is that the drilled ice cores were stored at the AWI facility for several years prior to CT imaging; during this period, sublimation and deposition processes may have closed or altered micro-scale pathways Bender et al. (1995); Li et al. (2026). Nevertheless, a resolution-related explanation can be discounted, as Schaller et al. (2017) conducted comparisons using much higher-resolution ($29\mu m$) data.

3.4 Modeling Transport Properties

Transport properties are sensitive to structural changes. As shown in Fig.10.b, both permeability and diffusivity exhibit relatively strong correlations with key microstructural features of pore network topology, geometry, and connectivity. The most important feature is open porosity for both transport properties with a correlation above 0.9, highlighting the central role of accessible pore space in facilitating flow and diffusion. Coordination number and its standard deviation also show high positive correlations with permeability, emphasizing the importance of a well-connected network of pores and throats for enabling gas transport through firn. Similarly, parameters such as mean pore volume, mean throat area, and mean pore surface area all contribute positively with a correlation of nearly 0.7, reinforcing the idea that larger and more numerous flow pathways strongly govern bulk transport efficiency. Throat-related parameters affect transport parameters slightly differently. Throat density has a higher correlation with diffusivity, whereas throat length has a higher correlation with permeability, meaning that more throats promote diffusion, but longer throats enhance permeability.

As the ice is in the progressive phase during the firnification process, with increasing MIL and spherical ice clusters, transport-related features drop significantly, so this feature has a huge negative correlation above 0.8. As the ice parts have higher ice clusters, the samples will have larger MIL, which weakens the transport properties. Also, anisotropy of MIL happens mostly on the convection range (Fig.7.d) therefore it has a higher correlation with permeability above 0.7 compared to

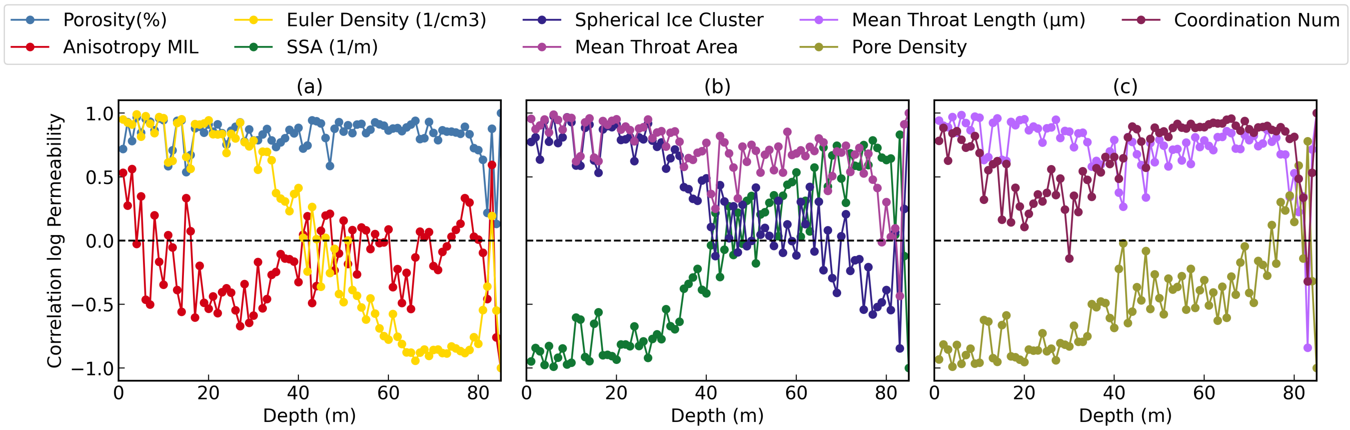

Figure 11. Feature correlation with log permeability per meter depth: a) geometrical properties, b,c) topological properties from Pore-Network model

diffusion (0.55). As diffusion is more sensitive to dead-end paths, cut porosity, isolated porosity, and cluster density, having significant negative correlations -0.75,-0.78,-0.9, respectively, with diffusivity.

In contrast, features such as isolated porosity and cluster density exhibit negative correlations, suggesting that fragmented or disconnected pore space reduces the effectiveness of flow pathways. Structural parameters, including specific surface area (SSA) and mean throat length, also show modest correlations, indicating that finer-scale surface and throat characteristics may modulate transport, but are not as dominant as porosity and connectivity (Fig. 10); however, these moderate parameters could be **depth related**, which needs further analysis in depth-wise.

Because firn densification is governed by a sequence of sintering stages beginning with grain rearrangement, neck growth, pore shrinkage, and capillary forces, its microstructural evolution is highly depth dependent. Each depth interval reflects a different balance of sintering forces: in the upper meters, overburden stress and grain settling dominate; at intermediate depths, vapor diffusion and temperature gradients control neck growth and pore connectivity, thus tracking the features per meter of depth is an important method to check the effect of each feature on transport parameters. Fig.11 shows the depth-dependent correlations between microstructural features and log(Permeability) across the firn column.

Porosity, coordination number, mean throat length, and area show strong positive correlations with permeability, indicating that large pore space and throats with many connections are primary positive controls on transport during the densification process (Fig.11). On the other hand, the Euler number and spherical ice cluster start with positive correlation at the surface (snow) and at the depth of $\sim 50m$ they switch to negative correlation. In contrast, SSA starts with a highly negative correlation, and after a depth of $50m$ it contributes positively to permeability. Similarly, pore density has a large negative correlation at the surface, and it rises till $\sim 70m$ and then becomes positively correlated. Anisotropy shows only moderate correlation, implying that structural directionality plays a limited role.

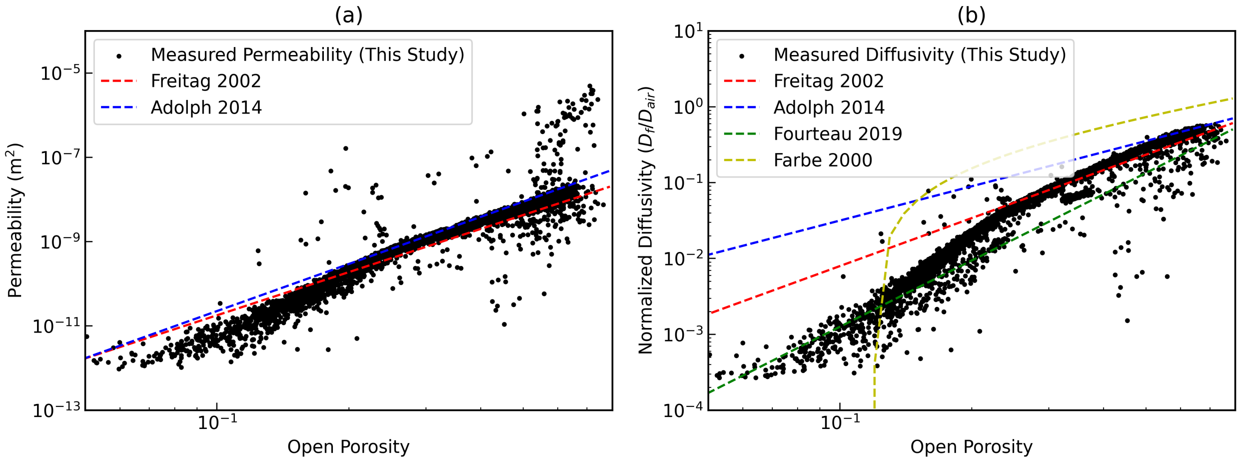

Figure 12. Permeability and normalized diffusivity on logarithmic scale in comparison with literature

As shown in Fig.12.a, the measured permeability and diffusivity values of the firn column of the current study exhibit clear trends when compared with empirical and theoretical models previously published in the literature. For permeability, our data align well with the Freitag et al. (2002) model over a broad range of open porosity values (ϕ), especially within the 0.2 to 0.6 range, and then it deviates from the models with open porosity less than 0.15, showing overestimation. In terms of diffusivity (Fig.12.b), the normalized diffusion coefficient (D/D_{air}) derived from our measurements shows notable consistency with the Freitag et al. (2002) and Fourteau et al. (2019) models across the open porosity spectrum up to approximately $\phi = 0.4$. The Freitag model captures the behavior well, particularly in the mid-porosity range. The Fourteau et al. (2019) model also tracks our data effectively, especially at the LIZ range, likely due to its foundation in Antarctic conditions, which may be more directly comparable to our dataset. Both of these models are using power laws (a line in the log-log plot), while our data is slightly curved downwards.

The Table.1 provides a structured overview of empirical and simulation-based models for firn permeability and normalized diffusivity, developed in prior studies that are used here for comparison with measurements of this study. Each model is formulated as a function of open porosity, reflecting the fundamental role of firn microstructure in controlling gas transport properties. The studies included were selected for their relevance and application to polar firn environments, and their parameterizations are also shown in the comparison figures for both permeability and diffusivity (Fig.12).

When compared with the present dataset, the Freitag et al. (2002) model tends to perform well in capturing both the curvature and magnitude of measured data for permeability with $R^2_{\log}$ of 0.90 and $RMSE_{\log}$ of 0.27 as well as normalized diffusion coefficient with $R^2_{\log}$ of 0.80 and $RMSE_{\log}$ of 0.29. The Adolph and Albert (2014) permeability formulation also agrees reasonably with the observations, performing slightly better than the Freitag model. However, their diffusivity model ($R^2_{\log}$ of 0.80) tends to overestimate values in the lower porosity regime observed in the current study (Fig.12).

Table 1. Summary of selected permeability and diffusivity models used for comparison.

Name	Formula	$R^2_{\log}$	$\mathrm{RMSE}_{\log}$	Remarks
Permeability				
Freitag et al. (2002)	$K = 10^{-7.7}\,\phi_{\mathrm{op}}^{1.5}$	0.90	0.27	$0.04 < \phi < 0.5$; from pore-scale simulations on samples from $16 to 57 m$ depth in North Greenland.
Adolph and Albert (2014)	$K = 10^{-7.29}\,\phi_{\mathrm{op}}^{2.71}$	0.91	0.25	$0.07 < \phi < 0.62$; from measurements on Summit (Greenland) firn.
Normalized Diffusion Coefficient				
Fabre et al. (2000)	$D/D_{\mathrm{air}} = 1.92\,\phi_{\mathrm{op}} - 0.23$	0.11	0.67	$0.15 < \phi < 0.4$; from measurements on Col du Dome (French Alps) and Vostok (Antarctica).
Freitag et al. (2002)	$D/D_{\mathrm{air}} = \phi_{\mathrm{op}}^{2.1}$	0.80	0.29	$0.04 < \phi < 0.5$; Simulations on North Greenland firn.
Adolph and Albert (2014)	$D/D_{\mathrm{air}} = \phi_{\mathrm{op}}^{1.5}$	0.23	0.59	$0.07 < \phi < 0.62$; from Summit (Greenland) firn measurements.
Fourteau et al. (2019)	$D/D_{\mathrm{air}} = \phi_{\mathrm{op}}^{2.9}$	0.69	0.37	$\phi < 0.2$; from Lock In (Antarctica) firn samples ($80\breve{}110 m$ depth).

The Fabre et al. (2000) model consistently over-predicts diffusivity (Fig.12), indicating limited applicability ($R^2_{\log}$ of 0.11) under colder and denser conditions, where pore tortuosity and connectivity reduce gas transport more drastically than linear scaling would suggest. By contrast, the Fourteau et al. (2019) model performs notably well in capturing the steep decrease in diffusivity as porosity falls below 0.2, a feature that aligns closely with the current data. This model has the overall $R^2_{\log}$ of 0.69 and $RMSE_{\log}$ of 0.37; however, its accuracy in the LIZ range is higher than that of other models, which highlights the importance of tailoring models to match the specific microstructural evolution of Antarctic firn sites, particularly as it transitions in various steps.

In sum, while all models provide useful insights into firn transport behavior, their performance varies depending on the environmental context in which they were developed. The Freitag et al. (2002) and Fourteau et al. (2019) models appear most robust when applied to the current data, likely because their formulations are grounded in either simulations or measurements from environments with comparable densification histories and climatic conditions. The Adolph and Fabre models are actually undefined for the lower porosity encountered here and can not be extrapolated beyond their original calibration zones, emphasizing the need for region-specific model development in firn air studies. This comparison also suggests that the denser, colder, and more slowly densifying firn of East Antarctica may not be well represented by models calibrated on Greenland conditions with higher temperature and densification rate.

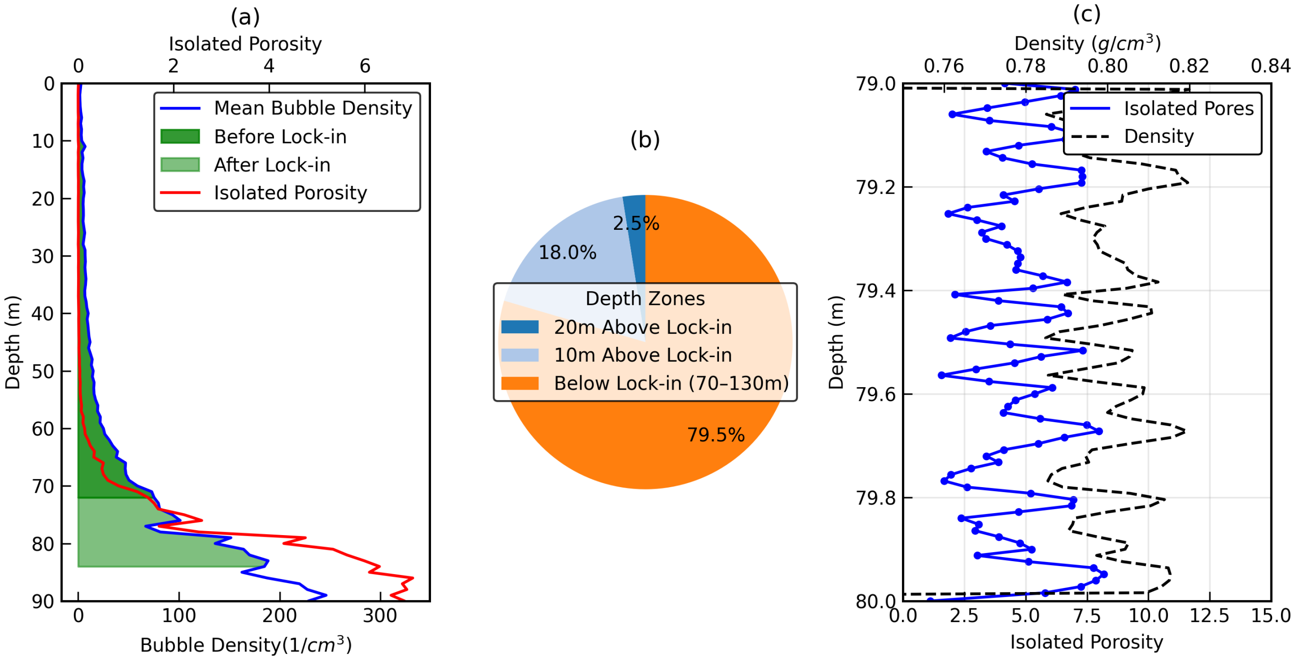

Figure 13. Entrapped air before pore close-off; a) closed bubbles volume; b) proportion of older air; c) 1-meter distribution with density

3.4.1 Early entrapped air

The illustration of the evolution of bubble density and isolated porosity in the ice core (Fig.13) provides insight into the timing of bubble closure relative to the pore close-off depth. As expected, mean bubble density increases progressively with depth (Fig.13.a), reflecting continuous firn densification and the gradual transition toward impermeable ice. However, the onset of isolated porosity occurs notably above the conventionally defined pore close-off depth. The increase in isolated porosity several meters before close-off indicates that a subset of bubbles seals earlier than predicted by bulk densification models, thereby trapping air that is older than the main air population at the close-off horizon.

The shaded regions (Fig.13.a) highlight this distinction: although the firn column remains partially permeable above the lock-in depth, isolated bubbles already begin to form. Once incorporated into the ice matrix, these early-closed bubbles contain air parcels that reflect atmospheric conditions from higher and older firn layers. Consequently, air extracted from bubbly ice represents a mixture of gases with different trapping ages reflecting the layered character in density rather than a single, discrete close-off age.

To quantify this behavior, the pie-chart distribution (Fig.13.b) shows that while the majority of bubbles originate from depths below lock-in, approximately 20% of the trapped air derives from $10\breve{}20m$ above the lock-in region. This contribution is substantial enough to broaden the gas-age distribution and introduces an older-air component to samples obtained by melt extraction. The early closure of bubbles is highly affected by density changes due to the stratigraphy of ice. These density

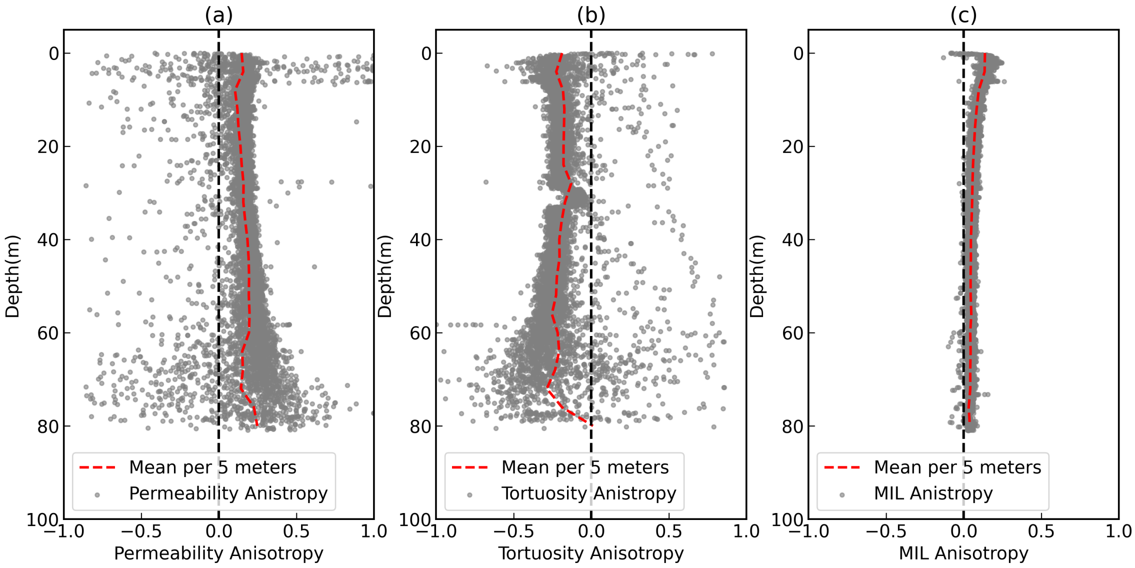

Figure 14. Anisotropy of the firn column, and color shows depth: a) permeability of void phase, b) tortuosity of void phase, c) mean intercept length (MIL) in ice phase

changes have a direct effect on developing these early trapped bubbles (Fig.13.c), where the denser layers contain more early trapped bubbles. These findings are consistent with the view that bubble closure in polar ice is not a sharply bounded process but instead spans a depth interval in which both permeable and isolated air coexist. This early closure mechanism has important implications for interpreting gas records from bubbly ice, particularly in contexts where high temporal precision is required.

3.4.2 Anisotropy

Anisotropy in firn and ice microstructure arises primarily from snow metamorphism under vertical temperature gradients and from uniaxial stress conditions experienced during densification under the weight of overlying snow layers. As firn compacts with depth, the vertical load causes pores and grains to rearrange preferentially along the Z axis, leading to enhanced connectivity and alignment in the vertical direction compared to the horizontal plane (Hörhold et al., 2009; Fourteau et al., 2023).

Fig.14.a compares permeability anisotropy as a function of depth. The anisotropy is calculated via Eq.3. Most values are clustered close to isotropy, but the fitted profile indicates a persistent positive anisotropy throughout the firn column, meaning that permeability in the vertical direction is generally higher than in the horizontal direction. The anisotropy is strongest near the surface, where values are more scattered, and the fitted curve reaches its maximum positive deviation. With increasing depth, the anisotropy remains positive but becomes more stable, suggesting that vertical pore connectivity is preserved during densification even as the pore space becomes progressively reduced. Near the pore close-off, the fitted curve shows a slight

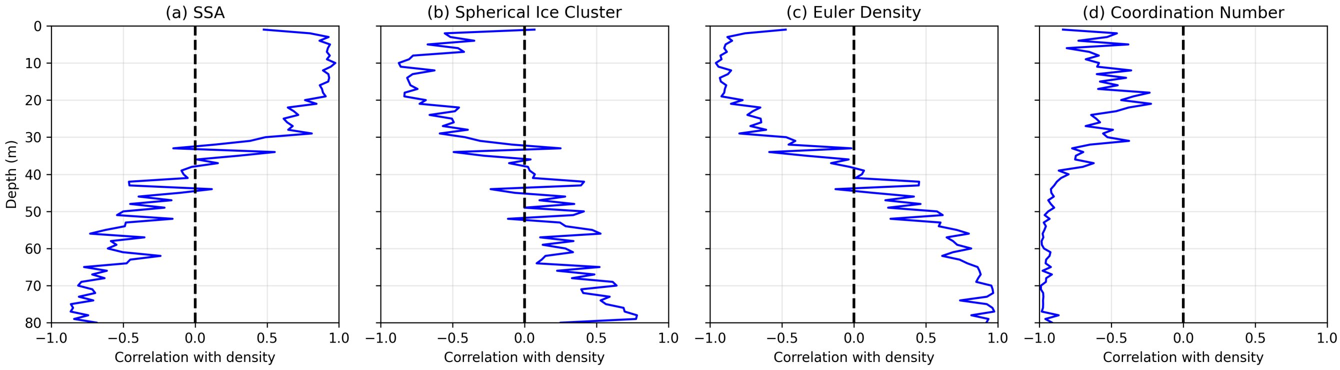

Figure 15. Correlation with density aggregated over per meter of depth for a) SSA; b) spherical ice cluster; c) Euler density; d) coordination number.

increase again, indicating localized enhancement of preferential vertical flow pathways. Similarly, Fig.14.b shows that the tortuosity anisotropy is the highest at the surface and near the pore close-off region.

Considering the ice phase, Fig.14.c presents the mean intercept length (MIL) anisotropy as a function of depth. Compared to permeability and tortuosity, MIL anisotropy is much weaker and remains close to isotropy throughout the profile. Nevertheless, the fitted curve consistently shows slightly positive values, indicating that the ice structure is marginally elongated in the vertical direction relative to the horizontal direction. The anisotropy is most evident near the surface and gradually decreases with depth, approaching near-isotropic conditions in the deeper firn and ice layers. However, it is worth noting that MIL is based on geometric length and, compared to transport properties, it is less sensitive to changes.

3.4.3 Fine Layer Detection

Fine layers in firn play a critical role in modulating firn densification, gas transport, and the preservation of paleo-climate signals. Previous studies (Freitag et al., 2004; Hörhold et al., 2011) have shown that stratigraphic variability within firn, such as the presence of thin fine-grained layers, strongly influences permeability, gas trapping, and the timing of bubble closure. Fine and coarse grains in a stratified ice structure densify differently.

This effect could be seen in the correlation between density and several densification indicators such as spherical ice cluster, SSA, Euler density, and coordination number along the depth (Fig.15). The strong correlation between density and these parameters in the top 20m of the core and then shifting the direction of correlation is a clear indication that the densification process of these layers is different at different depths. The correlation of density with spherical ice clusters is increasing in a negative direction till 20m and then shifting to a positive direction. This is also visible in the variability of porosity (Fig.5.a). One would expect that with increasing depth, the variability of porosity would be reduced, while it is shown in our dataset that after a depth of 40m, the variability is increasing till pore close-off depth.

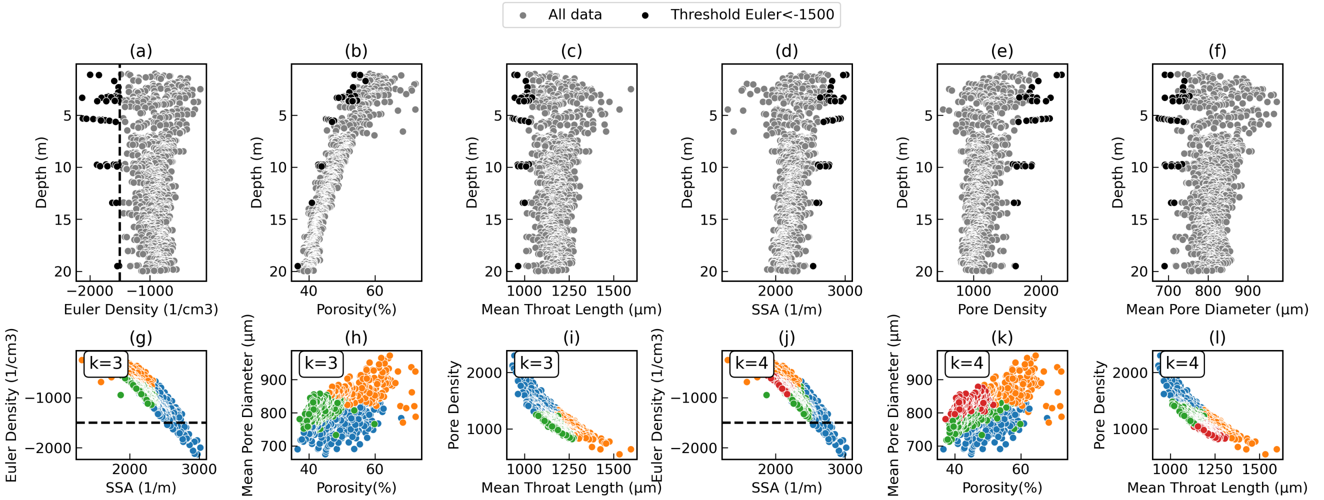

Figure 16. Detecting fine layers: a-f)thresholding with Euler density g-l) using K-means to identify potential clusters

Considering the top $20m$, fine layers are generally associated with higher density, reduced pore size, and lower permeability compared to coarser layers, thus forming semi-impermeable barriers that affect gas diffusion and retention. Identifying and quantifying these layers is therefore important for constraining firn air transport models and improving the interpretation of ice core records. However, after this depth, there would be a shift in correlation, which means the coarse-grained will have higher density. To identify the fine layers and avoid mixed signals, we focus on the top $20m$and set a threshold on microstructural parameters with respect to this range of depth.

As Fig.16.a-f presents microstructural features against depth for the top $20m$ of the firn column. Here, the Euler density was used with a threshold of $-1500cm^{-3}$ to distinguish regions with fine layers. Data points below this threshold (black dots) were then tracked across other microstructural properties to assess their consistency with the expected characteristics of fine layers. As expected, these fine layers, in comparison to the data points of the same depth, have lower porosity, shorter throats, smaller pore diameter, higher SSA, and pore density. It is well confirmed that the defined threshold has captured ideal fine layers. However, there is a possibility that there are finer layers that are harder to detect.

To identify the fine layers, we applied a k-means clustering approach using the measured microstructural parameters. To test the robustness of the clustering, we varied the number of clusters (three and four; Fig. 16.a–f). The fine layers (shown in blue) were consistently distinguished by their characteristic features, regardless of the chosen number of clusters. In comparison to other clusters, fine layers (blue cluster) have higher SSA and pore density with lower Euler density, porosity, and throat length.

Fig.17 shows the track of these clusters along the depth. These three clusters represent fine, coarse, and mixed layers. Fine layers are characterized by higher density and smaller pore sizes, while coarse layers display more open structures with larger pores and higher connectivity. The presence of mixed layers suggests zones where fine and coarse microstructures are interbedded or transitional. The vertical distribution (Fig.17) indicates that fine and coarse layers are mostly in the upper

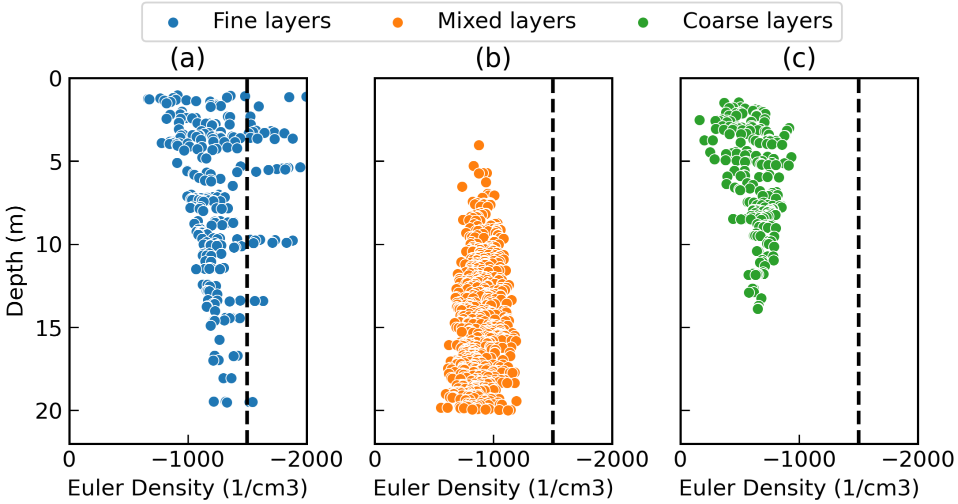

Figure 17. Layering clusters by depth a) fine layers b) mixed layers c) coarse layers

firn layers, and they change to mixed layers progressively. This transition is consistent with earlier findings that stratigraphic contrasts become less pronounced with depth due to overburden pressure and microstructural evolution, which gradually reduce the distinctiveness of layering. The mixed layers highlighted here represent intervals where fine and coarse structures are no 545 longer clearly separable, reflecting progressive firn compaction and the homogenizing effect of metamorphism (Hörhold et al., 2011).

3.4.4 Densification and Pore Network

As shown in Fig.18, network properties are changing with increasing depth. The number of pores shows a clear decreasing trend with increasing density (Fig.18.a). Initially, the number of pores fluctuates, likely due to microstructural variability at 550 low density, but as density surpasses 0.5 g/cm^3, the number of pores steadily declines. This reduction reflects the progressive elimination of voids during densification, as pore spaces collapse or merge under compaction forces, resulting in a denser material with fewer discrete pores. The number of clusters at higher densities illustrates a strong increase (Fig.18.b). This sharp rise indicates that as the porous network becomes more compressed, the remaining voids become increasingly isolated, forming numerous disconnected clusters. This fragmentation is a signature of advanced densification stages, where continuous 555 pathways are broken, and the pore network loses its percolation. Meanwhile, the mean pore diameter also decreases with density (Fig.18.c), suggesting that not only does the number of pores reduce, but the size of remaining pores contracts as well. The gradual decline in mean pore diameter aligns with physical expectations of pore collapse and compaction during sintering or compression (Arthern et al., 2010; Faria et al., 2017).

On the other hand, the mean throat diameter demonstrates a less pronounced but consistent decreasing trend as density in- 560 creases (Fig.18.d). This suggests that connections between pores, though less dramatically affected than the pores themselves,

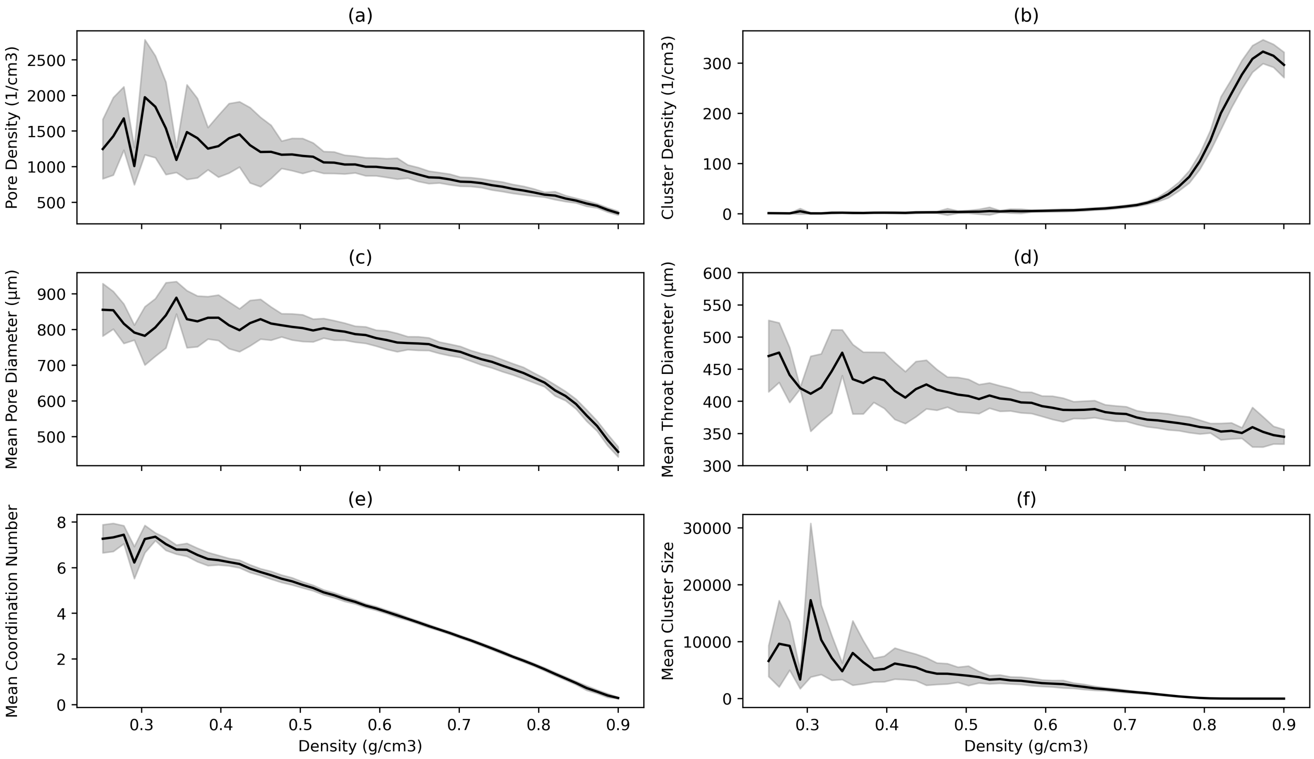

Figure 18. Density and pore network parameters; a) Pore density; b) Cluster density; c) Mean pore diameter; d) Mean throat diameter; e) Mean coordination number; f) Mean cluster size

also become narrower during densification. Similarly, confirms the compaction trend with coordination number steadily declining from over 7 to below 2 as density increases (Fig.18.e). A high coordination number at low density reflects a highly interconnected pore network, which diminishes under densification as pores become isolated. It is worth mentioning that the transition to impermeability is observed at a coordination number of around 1.6, which is in line with the theoretical threshold of percolation networks built by dodecahedral unit cells. It is experimental proof that the pore space of pressure-sintered ice structures behaves like a percolation network Stauffer (1989); Stauffer and Aharony (2018). Also, Fig.18.e shows that the mean cluster size decreases rapidly with density, especially in the range below 0.5 g/cm^3. This indicates that large interconnected pore networks disintegrate early in the densification process, giving way to numerous smaller and more isolated clusters at higher densities. Together, these plots depict a coherent densification process characterized by the reduction, fragmentation, and isolation of the pore structure.

In order to investigate the densification process by reducing the dimensionality of the dataset, the principal component analysis (PCA) of the pore network-related features was captured. It reveals how different microstructural features of the

https://doi.org/10.5194/egusphere-2026-3185
Preprint. Discussion started: 25 June 2026

porous medium relate to the densification process. To ensure the accuracy of the study, the missing values were dropped from the dataset before this analysis, and no scaling or feature selection was performed at this stage.

The first principal component (PC.1) captures the dominant trend in the dataset (Table.2), as indicated by the consistently high positive loadings across most pore-scale features. Variables such as coordination number, median number of connections, average pore diameter, volume, and surface area all contribute significantly and positively to PC.1. This suggests that PC.1 reflects the general size, connectivity, and geometric richness of the pore network structure. Notably, depth and density-related variables such as number of clusters and cluster density have negative loadings on PC.1, indicating that higher values of PC.1 correspond to more open, connected, and less dense pore networks. Therefore, PC.1 can be interpreted as a latent axis describing the transition from highly porous, interconnected structures to denser, fragmented ones as depth increases.

Table 2. Top feature loadings for the first three principal components (PC.1–PC.3). Significant contributions are shown in bold.

Features	**PC.1**	**PC.2**	**PC.3**
Coordination number	**0.2732**	-0.0891	0.0361
Median number of connections	**0.2664**	-0.1076	0.0814
Standard deviation of coordination number	**0.2642**	0.0123	0.1886
Average pore diameter	**0.2622**	0.0613	**-0.2625**
Average pore volume	**0.2612**	0.1707	-0.0863
Average pore surface area	**0.2608**	0.1251	**-0.2429**
Maximum cluster size	**0.2594**	**-0.1986**	0.0060
Average throat length	**0.2499**	**0.2112**	**-0.2172**
Number of throats	**0.2442**	**-0.2550**	**0.2731**
Number of pores	**0.2429**	**-0.2926**	0.1311
Average cluster size	0.2239	**-0.2653**	**0.3455**
Average throat area	0.1850	**0.5179**	0.2091
Maximum number of connections	0.1699	0.0330	**0.4350**
Average throat diameter	0.1351	**0.5919**	**0.2862**
Number of clusters	**-0.2512**	0.0258	**0.3446**
Cluster density	**-0.2512**	0.0258	**0.3446**
Explained Variance (%)	82.01	8.04	4.88

The second principal component (PC.2) shows a contrasting structure compared to PC.1. Here, the most dominant features include average throat diameter and average throat area, both of which have strong positive loadings. On the other hand, the number of pores, number of throats, and average cluster size have strong negative contributions (Table.2). This suggests that PC.2 captures variability in throat-related morphology, particularly throat dimensions, and distinguishes samples with wide, fewer throats from those with many, narrower throats. Additionally, the negative loading of maximum cluster size indicates that PC.2 also accounts for the extent of pore connectivity, though to a lesser degree. While PC.2 is not directly correlated

https://doi.org/10.5194/egusphere-2026-3185
Preprint. Discussion started: 25 June 2026

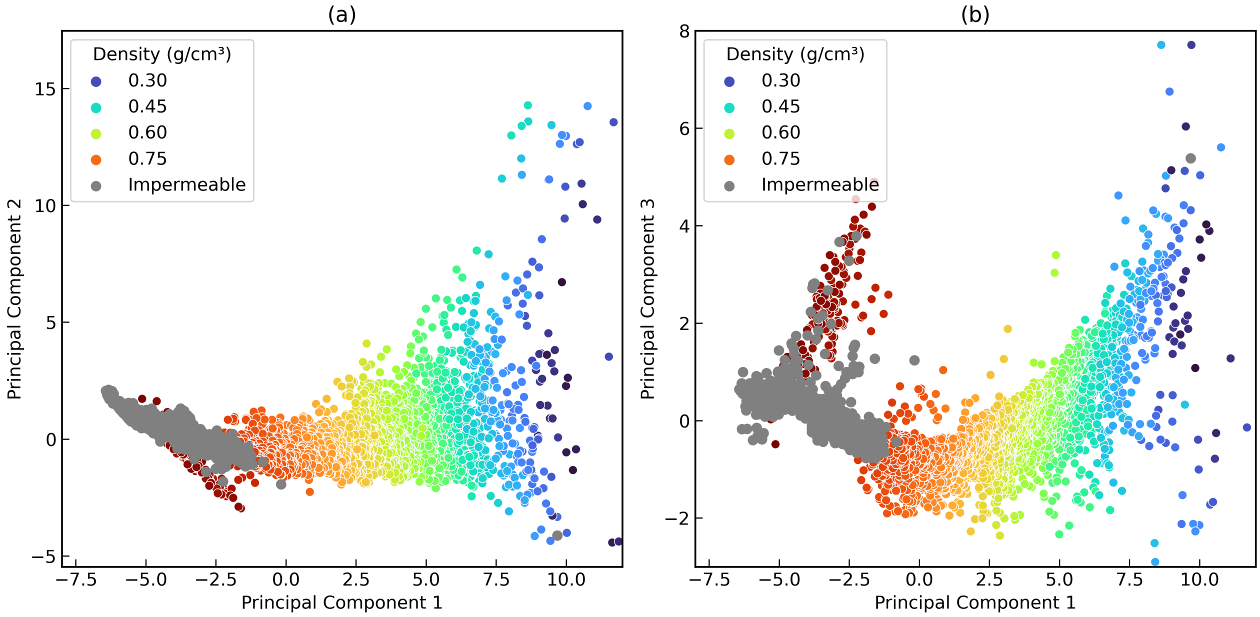

Figure 19. PCA with respect to density

with density, it likely encapsulates secondary structural differences in pore architecture that affect fluid transport and network anisotropy.

However, PC.3 presents a more complex set of relationships (Table.2), highlighting features associated with local connectivity and clustering behavior. Maximum number of connections, average cluster size, and cluster density all contribute strongly and positively to this component. These variables describe how concentrated and interconnected specific regions of the pore space are. At the same time, average pore surface area, average pore diameter, and average throat length show strong negative contributions to PC.3, suggesting that as local connectivity increases, the dimensions of individual features tend to decrease. This component may thus reflect localized densification phenomena, where high inter-connectivity coexists with small-scale geometrical constraints. The simultaneous presence of both positive and negative loadings with high magnitude underscores that PC.3 captures trade-offs within the pore network microstructure.

As shown in Fig.19, PC1 appears to capture a dominant trend in the dataset that correlates with density changes, which is visible with decreasing PC1 the density of samples increases. This supports the notion that PC1 is a reliable latent descriptor of the densification state. Features such as coordination number, pore volume, and pore diameter dominate PC1, suggesting that densification is accompanied by a decrease in connectivity and reduction of internal. The PCA loadings underscore that densification in this system is governed by multiple factors acting in combination, rather than a single dominant variable. For instance, coordination number and average pore volume both drive PC1 positively, meaning regions with more interconnected and voluminous pores are less dense (Table.2).

https://doi.org/10.5194/egusphere-2026-3185
Preprint. Discussion started: 25 June 2026

On the other hand, PC2 appears to distinguish samples based on localized variations in throat properties. Variables such as average throat diameter and average throat area have positive loadings in PC2, while average cluster size and number of pores have negative loadings (Table.2). This suggests PC2 might capture morphological heterogeneity in the throat structure rather than direct densification. The relatively weaker correlation of PC2 with density supports this interpretation, as the color gradient along the PC2 axis is less pronounced (Fig.19.a). PC2 has the highest variations with low-density samples, indicating that this axis would cover mostly the variations of snow samples.

However, PC3 is strongly influenced by the maximum number of connections, average cluster size, and cluster density, with positive loadings (Table.2), indicating that this component reflects variations in structural complexity and clustering behavior. Interestingly, average pore diameter and average throat length have significant negative contributions to PC3, suggesting a tradeoff between feature connectivity and geometric size (Fig.19.b). The shift in PC1 and PC3 space also reflects how clustering behaviors influence density (Fig.19.b). Features such as average cluster size and cluster density have notable roles in PC3, indicating that densely clustered pore networks alter the material's mechanical integrity and packing efficiency. This suggests that densification may proceed through the collapse or redistribution of these clusters, altering PC3 without significantly affecting PC1. The variation of PC3 in the outer range of densities ($\rho < 0.4$ and $\rho > 0.75$) that PC3 also tries to capture the variations on the top snow part and near pore-close-off part.

4 Conclusions

Ice cores from Antarctica preserve detailed records of past climate, atmospheric composition, and environmental changes over hundreds of thousands of years. Their microstructure, comprising pore geometry, grain size, and ice crystal connectivity, directly influences how gases are trapped and preserved, making it essential for the accurate interpretation of gas records. Understanding microstructural evolution helps reconstruct climate timelines and estimate the timing and rate of gas entrapment, crucial for studying ice atmosphere interactions. Studying these structures is vital for improving climate models and predicting future changes in polar and global systems.

This work demonstrates a robust and scalable workflow for recovering high-resolution microstructural parameters of ice cores from low-resolution micro-CT data using deep learning and pore network modeling. The integration of a super-resolution convolutional neural network with unsupervised segmentation and digital topology analysis enables reliable characterization of pore morphology, connectivity, and transport properties. The method was validated through physical weight comparisons and metrics such as PSNR and SSIM, and applied to a comprehensive analysis of the B40 ice core retrieved on the German research station Kohnen in Dronning Maud Land, East Antarctica, spanning snow, firn, and bubbly ice layers. The consistent alignment between measured and predicted physical parameters establishes confidence in the applicability of the approach across large datasets.

Our findings detail the continuous microstructural transformation occurring during firn densification. Geometrical and morphological descriptors, including porosity, specific surface area, Euler density, and mean intercept length, exhibit clear depth-dependent trends that reflect grain growth, pore collapse, and compaction processes. Pore network metrics such as coordination number and cluster size further capture the shift from open, connected structures to isolated, bubble-rich microenvironments, particularly within the lock-in and close-off depth ranges. It supports the application of the theoretical concept of percolation to the gradual pore close-off in natural polar firn. Transport modeling via OpenPNM shows a sharp decrease in permeability and an increase in tortuosity through this transition, with model results aligning closely with empirical formulations tailored to Antarctic conditions.

Through principal component analysis (PCA), we show that densification is governed by complex, multi-dimensional shifts in pore-scale structure, rather than changes in a single variable. The first PCA axis, strongly correlated with density, captures reductions in pore connectivity and feature size, while secondary components represent localized variations in throat morphology and clustering behavior. These findings highlight the utility of data-driven dimensionality reduction in interpreting microstructural evolution. The developed pipeline thus serves not only as a tool for detailed characterization but also as a bridge to unify machine learning, digital microstructure, and geophysical modeling in firn and ice research.

The key findings could be marked as:

- Super-resolution using ResNet architecture effectively reconstructs high-fidelity 3D microstructures from low-resolution ice core CT data, enabling detailed pore-scale analysis at large volumes.
- Empirical model validation of permeability and normalized diffusivity indicates best agreement of current data set with Antarctic-specific models (e.g., Freitag 2002, Fourteau 2019), underscoring the need for region-specific and depth-specific transport formulations in firn modeling.
- The correlation between spherical ice cluster size, specific surface area (SSA), and permeability changes direction with increasing depth.
- Almost 20%of the bubbles contain air that is older than the age obtained via pore close-off depth.
- Fine and coarse-grain layers could be identified with unsupervised clustering methods applied to microstructural features.
- The microstructural data support the idea of layer-specific densification rates resulting in a density crossover of fine and coarse-grained layers with depth.
- Impermeability occurs at a coordination number of 1.6, matching the predicted percolation threshold for dodecahedral networks, confirming that pressure-sintered ice behaves as a percolation system.
- Temperature gradient snow metamorphism induces vertical anisotropy in pore space and ice clusters. This anisotropy decreases with depth during densification but persists up to pore close-off, with slightly higher permeability and diffusivity in the vertical (Z) direction.
- PC analysis highlights variability in throat morphology and connectivity, suggesting that even at similar densities, samples may close off differently depending on local throat structure, influencing permeability behavior.

Future work will be focused on expanding this imaging and analysis pipeline to ice cores from diverse climatic regions, including Greenland, to compare microstructural evolution under different temperature and accumulation regimes. This would enable a broader understanding of regional differences in firn densification and gas trapping behavior. Additionally, coupling the derived microstructural data with other data sets (i.e., isotope, grain size, impurity load, dust, element and isotope ratios of firn air and enclosed gases) as well as physically based gas transport and firn densification models would allow for more accurate simulation of gas age–ice age differences and improve reconstructions of past atmospheric composition. Also, the clustering methods help to track similar samples across the depth and capture relevant events and their effect on firn evolution. Integrating these approaches could ultimately provide a unified, structure-informed framework for interpreting gas records across polar ice sheets.

Code and data availability. The programming language of this study was Python, along with various libraries: Numpy, Pandas, OpenCV, skimage, tiff, patchify, SimpleITK, SKlearn, Scipy, Pytorch, PuMA, PoresPy, OpenPNM, and matplotlib.
The code used for this study is available: https://github.com/B40_SR_microstructure. The microstructure analysis dataset is attached to this manuscript. The raw image data ($\approx$ 1 TB) and processed data, including super-resolution and segmentation files ($\approx$ 8 TB), could be provided upon individual request to Dr.Johannes Freitag (Johannes.Freitag@awi.de). However, a sample of the raw image data, which was initially used, is available Bagherzadeh and Freitag (2024), https://dx.doi.org/10.21227/abw4-7c19.

Author contributions. Faramarz Bagherzadeh: Writing the manuscript and computer programming. Johannes Freitag: prepared core samples, performed micro-CT scanning, and contributed to the code and manuscript. Udo Frese: developed computer science ideas and contributed to the manuscript. Frank Wilhelms: developed Glaciology ideas and contributed to the manuscript.

Declaration of generative AI: During the preparation of this work, the authors used Grammarly, QuillBot, and ChatGPT to do text polishing. After using these tools, the authors reviewed and edited the content as needed and took full responsibility for the content of the publication.

Competing interests. The authors declare no conflict of interest.

Acknowledgements. We acknowledge the support of the Open Access Publication Funds of Alfred-Wegener-Institut Helmholtz-Zentrum für Polar- und Meeresforschung. Also, the first author (Faramarz Bagherzadeh) is funded through the Helmholtz School for Marine Data Science (MarDATA), Grant No. HIDSS-0005. We would like to appreciate the work of Ice Lab assistants Jakob Rieger and Sören Geil regarding ice handling and X-ray imaging.

https://doi.org/10.5194/egusphere-2026-3185
Preprint. Discussion started: 25 June 2026

References

Adolph, A. C. and Albert, M. R.: Gas diffusivity and permeability through the firn column at Summit, Greenland: measurements and comparison to microstructural properties, The Cryosphere, 8, 319–328, 2014.

Arnaud, L., Lipenkov, V., Barnola, J.-M., Gay, M., and Duval, P.: Modelling of the densification of polar firn: characterization of the snow–firn transition, Annals of Glaciology, 26, 39–44, 1998.

Arthern, R. J., Vaughan, D. G., Rankin, A. M., Mulvaney, R., and Thomas, E. R.: In situ measurements of Antarctic snow compaction compared with predictions of models, Journal of Geophysical Research: Earth Surface, 115, 2010.

Bagherzadeh, F. and Freitag, J.: 3D super resolution micro CT for ice cores, https://doi.org/10.21227/abw4-7c19, 2024.

Bagherzadeh, F., Freitag, J., Frese, U., and Wilhelms, F.: Ice-core micro-CT image segmentation with deep learning and Gaussian mixture model, IEEE Transactions on Geoscience and Remote Sensing, 61, 1–11, 2023.

Bagherzadeh, F., Freitag, J., Frese, U., Tavousi, P., and Wilhelms, F.: Resolution Enhancement of Polar Ice Core Micro CT Scans via Deep Learning: A Comparative Study, IEEE Access, 12, 175 666–175 679, https://doi.org/10.1109/ACCESS.2024.3504726, 2024a.

Bagherzadeh, F., Freitag, J., Frese, U., and Wilhelms, F.: Resolution enhancement and segmentation of polar bubbly ice micro CT scans via 3D convolutional neural network, Applied Computing and Geosciences, 23, 100 193, 2024b.

Bagherzadeh, F., Freitag, J., Frese, U., and Wilhelms, F.: Resolution enhancement and segmentation of polar bubbly ice micro CT scans via 3D convolutional neural network, Applied Computing and Geosciences, 23, 100 193, 2024c.

Barbante, C., Fischer, H., Masson-Delmotte, V., Waelbroeck, C., and Wolff, E. W.: Climate of the last million years: new insights from EPICA and other records, Quaternary Science Reviews, 29, 1–7, 2010.

Battle, M., Severinghaus, J., Sofen, E., Plotkin, D., Orsi, A., Aydin, M., Montzka, S., Sowers, T., and Tans, P.: Controls on the movement and composition of firn air at the West Antarctic Ice Sheet Divide, Atmospheric Chemistry and Physics, 11, 11 007–11 021, 2011.

Bendel, V., Ueltzhöffer, K. J., Freitag, J., Kipfstuhl, S., Kuhs, W. F., Garbe, C. S., and Faria, S. H.: High-resolution variations in size, number and arrangement of air bubbles in the EPICA DML (Antarctica) ice core, Journal of Glaciology, 59, 972–980, 2013.

Bender, M., Sowers, T., and Lipenkov, V.: On the concentrations of O2, N2, and Ar in trapped gases from ice cores, Journal of Geophysical Research: Atmospheres, 100, 18 651–18 660, 1995.

Bender, M. L.: Orbital tuning chronology for the Vostok climate record supported by trapped gas composition, Earth and Planetary Science Letters, 204, 275–289, 2002.

Bouvet, L., Calonne, N., Flin, F., and Geindreau, C.: Heterogeneous grain growth and vertical mass transfer within a snow layer under a temperature gradient, The Cryosphere, 17, 3553–3573, 2023.

Bréant, C., Martinerie, P., Orsi, A., Arnaud, L., and Landais, A.: Modelling firn thickness evolution during the last deglaciation: constraints on sensitivity to temperature and impurities, Climate of the Past, 13, 833–853, 2017.

Buizert, C.: The ice core gas age-ice age difference as a proxy for surface temperature, Geophysical Research Letters, 48, e2021GL094 241, 2021.

Calonne, N., Burr, A., Philip, A., Flin, F., and Geindreau, C.: Effective coefficient of diffusion and permeability of firn at Dome C and Lock In, Antarctica, and of various snow types–estimates over the 100–850 kg m- 3 density range, The Cryosphere, 16, 967–980, 2022.

Çiftçioğlu, A. Ö., Delikanlı, A., Shafighfard, T., and Bagherzadeh, F.: Machine learning based shear strength prediction in reinforced concrete beams using Levy flight enhanced decision trees, Scientific Reports, 15, 27 488, 2025.

Cuffey, K. M. and Paterson, W. S. B.: The physics of glaciers, Academic Press, 2010.

Fabre, A., Barnola, J.-M., Arnaud, L., and Chappellaz, J.: Determination of gas diffusivity in polar firn: Comparison between experimental measurements and inverse modeling, Geophysical research letters, 27, 557–560, 2000.

Faria, S. H., Kipfstuhl, S., and Lambrecht, A.: The EPICA-DML deep ice core: A visual record, Springer, 2017.

Ferguson, J. C., Panerai, F., Borner, A., and Mansour, N. N.: PuMA: The porous microstructure analysis software, SoftwareX, 7, 81–87, 2018.

Ferguson, J. C., Semeraro, F., Thornton, J. M., Panerai, F., Borner, A., and Mansour, N. N.: Update 3.0 to "PuMA: The Porous Microstructure Analysis software",(PII: S2352711018300281), SoftwareX, 15, 100 775, 2021.

Fourteau, K., Martinerie, P., Faïn, X., Schaller, C. F., Tuckwell, R. J., Löwe, H., Arnaud, L., Magand, O., Thomas, E. R., Freitag, J., et al.: Multi-tracer study of gas trapping in an East Antarctic ice core, The Cryosphere, 13, 3383–3403, 2019.

Fourteau, K., Freitag, J., Malinen, M., and Löwe, H.: Microstructure-based simulations of the viscous densification of snow and firn, EGUsphere, 2023, 1–26, 2023.

Freitag, J., Dobrindt, U., and Kipfstuhl, J.: A new method for predicting transport properties of polar firn with respect to gases on the pore-space scale, Annals of Glaciology, 35, 538–544, 2002.

Freitag, J., Wilhelms, F., and Kipfstuhl, S.: Microstructure-dependent densification of polar firn derived from X-ray microtomography, Journal of Glaciology, 50, 243–250, 2004.

Freitag, J., Kipfstuhl, S., Laepple, T., and Wilhelms, F.: Impurity-controlled densification: a new model for stratified polar firn, Journal of Glaciology, 59, 1163–1169, 2013.

Gackiewicz, B., Lamorski, K., Sławiński, C., Hsu, S.-Y., and Chang, L.-C.: An intercomparison of the pore network to the Navier–Stokes modeling approach applied for saturated conductivity estimation from X-ray CT images, Scientific reports, 11, 5859, 2021.

Gostick, J., Aghighi, M., Hinebaugh, J., Tranter, T., Hoeh, M. A., Day, H., Spellacy, B., Sharqawy, M. H., Bazylak, A., Burns, A., Lehnert, W., and Putz, A.: OpenPNM: A Pore Network Modeling Package, Computing in Science and Engineering, 18, 60–74, https://doi.org/10.1109/MCSE.2016.49, 2016.

Gostick, J. T.: Versatile and efficient pore network extraction method using marker-based watershed segmentation, Physical Review E, 96, 023 307, 2017.

Gostick, J. T., Khan, Z. A., Tranter, T. G., Kok, M. D., Agnaou, M., Sadeghi, M., and Jervis, R.: PoreSpy: A Python Toolkit for Quantitative Analysis of Porous Media Images, Journal of Open Source Software, 4, 1296, https://doi.org/10.21105/joss.01296, 2019.

Gregory, S., Albert, M., and Baker, I.: Impact of physical properties and accumulation rate on pore close-off in layered firn, The Cryosphere, 8, 91–105, 2014.

Hagenmuller, P., Chambon, G., Lesaffre, B., Flin, F., and Naaim, M.: Energy-based binary segmentation of snow microtomographic images, Journal of Glaciology, 59, 859–873, 2013.

Heggli, M., Frei, E., and Schneebeli, M.: Snow replica method for three-dimensional X-ray microtomographic imaging, Journal of Glaciology, 55, 631–639, 2009.

Heggli, M., Köchle, B., Matzl, M., Pinzer, B., Riche, F., Steiner, S., Steinfeld, D., and Schneebeli, M.: Measuring snow in 3-D using X-ray tomography: assessment of visualization techniques, Annals of Glaciology, 52, 231–236, 2011.

Herron, M. M. and Langway Jr, C. C.: Firn densification: an empirical model, Journal of Glaciology, 25, 373–385, 1980.

Hoffmann-Abdi, K., Fernandoy, F., Meyer, H., Freitag, J., Opel, T., McConnell, J. R., and Schneider, C.: Short-term meteorological and environmental signals recorded in a firn core from a high-accumulation site on plateau Laclavere, Antarctic Peninsula, Geosciences, 11, 428, 2021.

Hörhold, M., Kipfstuhl, S., Wilhelms, F., Freitag, J., and Frenzel, A.: The densification of layered polar firn, Journal of Geophysical Research: Earth Surface, 116, 2011.

Hörhold, M., Münch, T., Weißbach, S., Kipfstuhl, S., Freitag, J., Sasgen, I., Lohmann, G., Vinther, B., and Laepple, T.: Modern temperatures in central–north Greenland warmest in past millennium, Nature, 613, 503–507, 2023.

Hörhold, M. W., Albert, M. R., and Freitag, J.: The impact of accumulation rate on anisotropy and air permeability of polar firn at a high-accumulation site, Journal of Glaciology, 55, 625–630, 2009.

Jouzel, J., Masson-Delmotte, V., Cattani, O., Dreyfus, G., Falourd, S., Hoffmann, G., Minster, B., Nouet, J., Barnola, J.-M., Chappellaz, J., et al.: Orbital and millennial Antarctic climate variability over the past 800,000 years, science, 317, 793–796, 2007.

Kawamura, K., Severinghaus, J. P., Ishidoya, S., Sugawara, S., Hashida, G., Motoyama, H., Fujii, Y., Aoki, S., and Nakazawa, T.: Convective mixing of air in firn at four polar sites, Earth and Planetary Science Letters, 244, 672–682, 2006.

Kerckhofs, G., Schrooten, J., Van Cleynenbreugel, T., Lomov, S. V., and Wevers, M.: Validation of x-ray microfocus computed tomography as an imaging tool for porous structures, Review of Scientific Instruments, 79, 2008.

Kipfstuhl, S., Faria, S. H., Azuma, N., Freitag, J., Hamann, I., Kaufmann, P., Miller, H., Weiler, K., and Wilhelms, F.: Evidence of dynamic recrystallization in polar firn, Journal of Geophysical Research: Solid Earth, 114, 2009.

Li, Q., Hu, H., Shi, G., Wang, D., Li, Z., and Hou, S.: Gas loss and isotopic fractionation induced by pumping during ice core gas extractions, EGUsphere, 2026, 1–17, 2026.

Martinerie, P., Raynaud, D., Etheridge, D. M., Barnola, J.-M., and Mazaudier, D.: Physical and climatic parameters which influence the air content in polar ice, Earth and Planetary Science Letters, 112, 1–13, 1992.

Misaghian, M., Bagherzadeh, F., and Bałachowski, L.: Comparative study on data-driven prediction of overconsolidation ratio using supervised machine learning models, Frontiers of Structural and Civil Engineering, 19, 1192–1201, 2025.

Opel, T., Fritzsche, D., Meyer, H., Schütt, R., Weiler, K., Ruth, U., Wilhelms, F., and Fischer, H.: 115 year ice-core data from Akademii Nauk ice cap, Severnaya Zemlya: high-resolution record of Eurasian Arctic climate change, Journal of Glaciology, 55, 21–31, 2009.

Raynaud, D., Jouzel, J., Barnola, J., Chappellaz, J., Delmas, R., and Lorius, C.: The ice record of greenhouse gases, Science, 259, 926–934, 1993.

Rizi, R. A., Bagherzadeh, F., Schnabel, M. A., and Bakshi, N.: A design methodology to consider occupants' spatial adjustment and manage view content in adaptive façade design for improving visual comfort, Architectural Engineering and Design Management, 20, 168–190, 2024.

Salamatin, A. N. and Lipenkov, V. Y.: Simple relations for the close-off depth and age in dry-snow densification, Annals of Glaciology, 49, 71–76, 2008.

Schaller, C. F., Freitag, J., and Eisen, O.: Critical porosity of gas enclosure in polar firn independent of climate, Climate of the Past, 13, 1685–1693, 2017.

Sigl, M., Jenk, T. M., Kellerhals, T., Szidat, S., Gäggeler, H., Wacker, L., Synal, H.-A., Boutron, C., Barbante, C., Gabrieli, J., et al.: Towards radiocarbon dating of ice cores, Journal of Glaciology, 55, 985–996, 2009.

Sigl, M., McConnell, J. R., Toohey, M., Curran, M., Das, S. B., Edwards, R., Isaksson, E., Kawamura, K., Kipfstuhl, S., Krüger, K., et al.: Insights from Antarctica on volcanic forcing during the Common Era, Nature Climate Change, 4, 693–697, 2014.

Stauffer, D.: Classification of square lattice cellular automata, Physica A: Statistical Mechanics and its Applications, 157, 645–655, 1989.

Stauffer, D. and Aharony, A.: Introduction to percolation theory, Taylor & Francis, 2018.

https://doi.org/10.5194/egusphere-2026-3185
Preprint. Discussion started: 25 June 2026

Su, H., Li, Y., Xu, Y., Fu, X., and Liu, S.: A review of deep-learning-based super-resolution: From methods to applications, Pattern Recognition, p. 110935, 2024.

Umirzakova, S., Ahmad, S., Khan, L. U., and Whangbo, T.: Medical image super-resolution for smart healthcare applications: A comprehensive survey, Information Fusion, 103, 102 075, 2024.

Voland, V., Müller, A., Firsching, M., Gruber, R., Mohr, S., Habl, M., Schön, T., Oeckl, S., Schröpfer, S., Hess, J., et al.: Computed tomography (CT) system for automatic analysis of ice cores, in: European Conference on Non-Destructive Testing (ECNDT) 2010, 2010.

Wagner, A., Eggenweiler, E., Weinhardt, F., Trivedi, Z., Krach, D., Lohrmann, C., Jain, K., Karadimitriou, N., Bringedal, C., Voland, P., et al.: Permeability estimation of regular porous structures: A benchmark for comparison of methods, Transport in porous media, 138, 1–23, 2021.

Weiler, K.: On the Composition of Firn Air and its Dependence on Seasonally Varying Atmospheric Boundary Conditions and the Firn Structure, Phd thesis, University of Bern, Bern, Switzerland, 2008.

Weinhart, A. H., Freitag, J., Hörhold, M., Kipfstuhl, S., and Eisen, O.: Representative surface snow density on the East Antarctic Plateau, The Cryosphere Discussions, 2020, 1–26, 2020.